

Review

Recent Advance in Nucleus-Targeted Fluorescent Probes for Bioimaging, Detection and Therapy

Cong Hu ¹, Shuai Xu ^{2,*}, Zhiling Song ³, Haixia Li ¹ and Hongwen Liu ^{1,*} 

¹ Key Laboratory of Chemical Biology and Traditional Chinese Medicine Research, College of Chemistry and Chemical Engineering, Hunan Normal University, Changsha 410082, China

² School of Chemistry and Chemical Engineering, University of Jinan, Jinan 250022, China

³ Shandong Key Laboratory of Biochemical Analysis, College of Chemistry and Molecular Engineering, Qingdao University of Science and Technology, Qingdao 266042, China

* Correspondence: chm_xus@ujn.edu.cn (S.X.); liuhongwen@hnu.edu.cn (H.L.)

Abstract: The nucleus is not only the control hub of cell life activities, but also the center of storing and controlling genetic information. The morphology of the nucleus can be used to judge the cell vitality and health. The various biological molecules contained in the nucleus are closely related to the normal life activities, occurrence and development of diseases. In recent years, fluorescence imaging has gained increasing attention due to its advantages of being intuitive, in situ and visual. The development of fluorescent probes for high-resolution imaging of the nucleus and detection of biomolecules in the nucleus is of great value for understanding the normal physiological processes of cells or organisms, as well as for disease diagnosis and treatment. In this review, we mainly introduce the current general strategies for designing nucleus-targeted fluorescent probes, as well as their applications in nucleus-targeted imaging, intranuclear biomolecular detection and therapy. Moreover, we also discuss the current challenges and opportunities of nucleus-targeted fluorescent probes in terms of selectivity, design strategies and so on.

Keywords: nucleus-targeted; fluorescent probes; bioimaging; detection; therapy



Citation: Hu, C.; Xu, S.; Song, Z.; Li, H.; Liu, H. Recent Advance in Nucleus-Targeted Fluorescent Probes for Bioimaging, Detection and Therapy. *Chemosensors* **2023**, *11*, 125. <https://doi.org/10.3390/chemosensors11020125>

Academic Editor: Mark Lowry

Received: 30 December 2022

Revised: 1 February 2023

Accepted: 6 February 2023

Published: 7 February 2023



Copyright: © 2023 by the authors. Licensee MDPI, Basel, Switzerland. This article is an open access article distributed under the terms and conditions of the Creative Commons Attribution (CC BY) license (<https://creativecommons.org/licenses/by/4.0/>).

1. Introduction

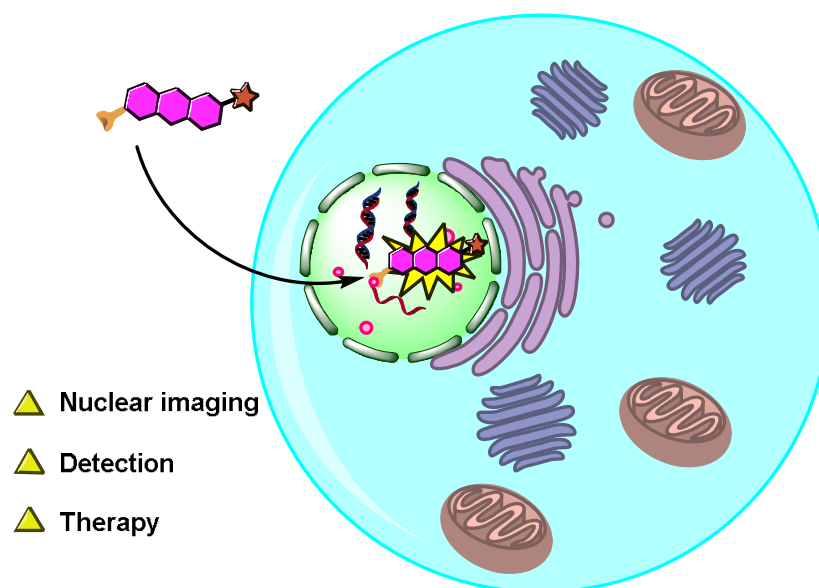
The nucleus, a highly specialized subcellular organelle, is the largest and most important cellular structure within eukaryotic cells [1]. The nucleus, as the “heart” of the cell, is a storage site for genetic information and is a control center of the cell. Gene replication, transcription, and processing of transcribed primaries, are all associated with the nucleus. The nucleus consists of the nuclear membrane, nuclear lamina, chromatin, nucleolus and nuclear body, among others. The nuclear membrane consists of a bilayer containing protein and phospholipid molecules, and a large number of nuclear pores are present at the membrane surface. Nuclear pore is a selective hydrophilic channel. Small molecules (such as ions, metabolites, etc.) pass through the nuclear pore by simple diffusion, while macromolecules (such as proteins, RNA, ribosomal subunits, etc.) need to be transported by active transport under the guidance of nuclear translocation signals and transport carriers. Chromatin is the existing form of genetic material inside the cell and mainly consists of DNA and histone. Chromatin also contains a few RNA, which are equally important for the normal function of chromatin. The nucleolus is mainly composed of RNA and proteins, and its altered function manifests as aberrant ribosome biogenesis or nucleolar stress, which can induce various diseases [2]. Therefore, it is very important to monitor the morphological changes and the biological events in the nucleus, and it will be of great interest to understand the situation of cell viability and normal physiological activities.

Fluorescent imaging of the nucleus is one of the most important tasks in bioimaging research, and it is beneficial to study cell growth and development, nucleic acid quantification and dynamic changes and cancer therapy, etc. By imaging the nucleus, the spatiotemporal

changes in the nucleus, such as chromosome segregation during mitosis, could be observed in real time and in situ. In addition, the detection of biomolecules in the nucleus also has high research value. The nucleus contains a variety of biomolecules, such as anions, metal cations, reactive oxygen/reactive nitrogen species (ROS/RNS), small molecules and biomacromolecules, are closely related to the normal physiological and pathological activities of the cells. In recent years, studies have shown that the abnormal expression of nucleic acids and some enzymes within the nucleus are the main causes of cellular carcinogenesis and malignant proliferation [3,4]. Since the key function of the nucleus, the nucleus-targeted therapy may achieve high therapeutic efficacy. Photodynamic therapy (PDT) is currently an effective method for the treatment of cancer. The labile ROS generated by PDT can easily damage nucleic acids within the nucleus and the development of nucleus-targeted therapy can decrease the probability of these ROS reductions by the large amount of glutathione (GSH) in the cytoplasm, which will contribute to highly effective cancer therapy. Therefore, the nucleus-targeted therapy may be one of the most effective ways to treat cancer. Briefly, considering the importance of the nucleus and intranuclear biomolecules to the cell, achieving highly sensitive and selective imaging and detection of various biomolecules in the nucleus is beneficial to understand the normal physiological and pathological processes of cells or organisms, and facilitate the diagnosis and treatment of related diseases.

Although high-performance liquid chromatography (HPLC) and mass spectrometry (MS) have been widely used for the detection of various biomolecules in organelles so far [5], these two methods require the separation of organelles, and more importantly, they cannot be used for real-time monitoring of biomolecules in living cells. As an intuitive, in situ and visual technique, fluorescence imaging has been widely used for labeling and detection of functional molecules. Due to the specificity of nuclear pores, it is always a difficult problem for small molecular probes or other exogenous organic molecules to enter the nucleus via the nuclear pores. With appropriate modifications, small-molecule probes enable specific targeting of the nucleus. Relative to nano fluorescent probes, small-molecule fluorescent probes are capable of detecting various biological targets due to their structural tailorability. Therefore, small-molecule fluorescent probes have become a powerful tool to real-time detect and image biological events in the nucleus, enabling the revelation and investigation of the nucleus functions [6,7]. However, since this approach requires the construction of nucleus-targeted fluorescent probes, it comes with the challenges of sensitive and selective imaging and detection in the nucleus. First, once the probes do not have suitable nuclear transport signals or carriers, they can hardly enter the nucleus. Moreover, a large number of nucleic acids are abundant in the nucleus. Once the probe enters the nucleus, it may affect the normal function of the nucleus or even lead to cell death. Moreover, the targeting specificity of fluorescent probes is also a matter worth considering. To address these challenges, in the past years, great efforts have been devoted to the development of real-time and highly sensitive small-molecule fluorescent probes to detect and image in the nucleus.

In this review, we mainly introduce the small-molecule fluorescent probes that have been developed over the past two decades (Scheme 1). Nanomaterials are also briefly discussed. We first summarize two currently common strategies for the design of nucleus-targeted fluorescent probes utilizing commercial nucleus targeting dyes and nuclear localization signal (NLS) peptides. The possible mechanism of nucleus-targeted probes into the nucleus is also discussed. Subsequently, we introduce in detail the fluorescent probes developed in recent years that can be used for nuclear imaging and nuclear biomolecule detection. Moreover, we present the applications of nucleus-targeted fluorescent probes in medical treatment from the aspects of PDT therapy and improving the nucleus-targeted delivery efficiency of drugs or probes. Finally, the current challenges and the potential future directions, which would evoke more research interest and open new avenues for biological analysis of the nucleus, are included as well.



Scheme 1. Small-molecule fluorescent probes are used for nuclear imaging, detection and therapy.

2. Representative General Strategies for Constructing Nucleus-Targeting Probes

There are two main strategies for the design of organelle targeted fluorescent probes: chemical molecular labeling and fusion protein tagging. At present, the general design strategy of a nucleus-targeted fluorescent probe is mainly the chemical molecular labeling method. The chemical molecular labeling method is one way to achieve organelle targeting by covalently linking fluorescent probes and organelle targeting units, such as some natural and synthetic peptides and some small molecules (Figure 1). When designing nucleus-targeted fluorescent probes, the lipophilicity, hydrophilicity and charge density of the probes must be considered comprehensively. These properties of probe molecules are closely related to the cell penetration ability and nuclear targeting ability [8].

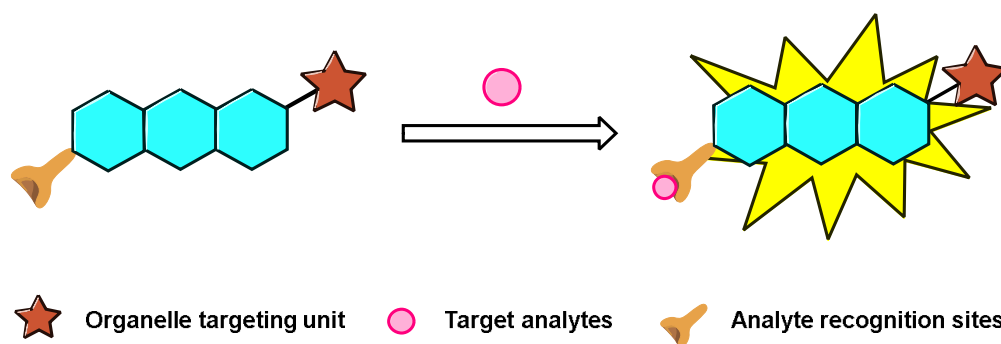


Figure 1. Schematic representation of the chemical molecular labelling method.

2.1. Nucleus Targeting Dye

At present, the design of nucleus-targeted fluorescent probes is mainly aimed at the large amount of negatively charged DNA contained in the nucleus, which is achieved by introducing hydrophilic cations. Taking advantage of the feature that hydrophilic cations in probes together with negatively charged DNA can tightly combine with each other through electrostatic interactions [9], many nucleus-targeted probes have been developed. These probes generally contain short hydrophobic chains and planar aromatic cationic structures. For example, Hoechst, DAPI and SYBR Green 1, commonly used commercial nucleus fluorescent dyes, possess the above characteristics and their structures are shown in the Figure 2a, these dyes can selectively bind to double stranded DNA (dsDNA) at the minor groove [10,11]. The design strategy for generating nucleus-targeted fluorescent

probes is to use the above commercial nuclei fluorescent dyes as the nucleus targeting group, and combine with other fluorescent probes by a flexible long chain to form novel nucleus-targeted probes. For example, Figure 2b demonstrates a general strategy to design nucleus-targeted fluorescent probes utilizing Hoechst-tagging [12].

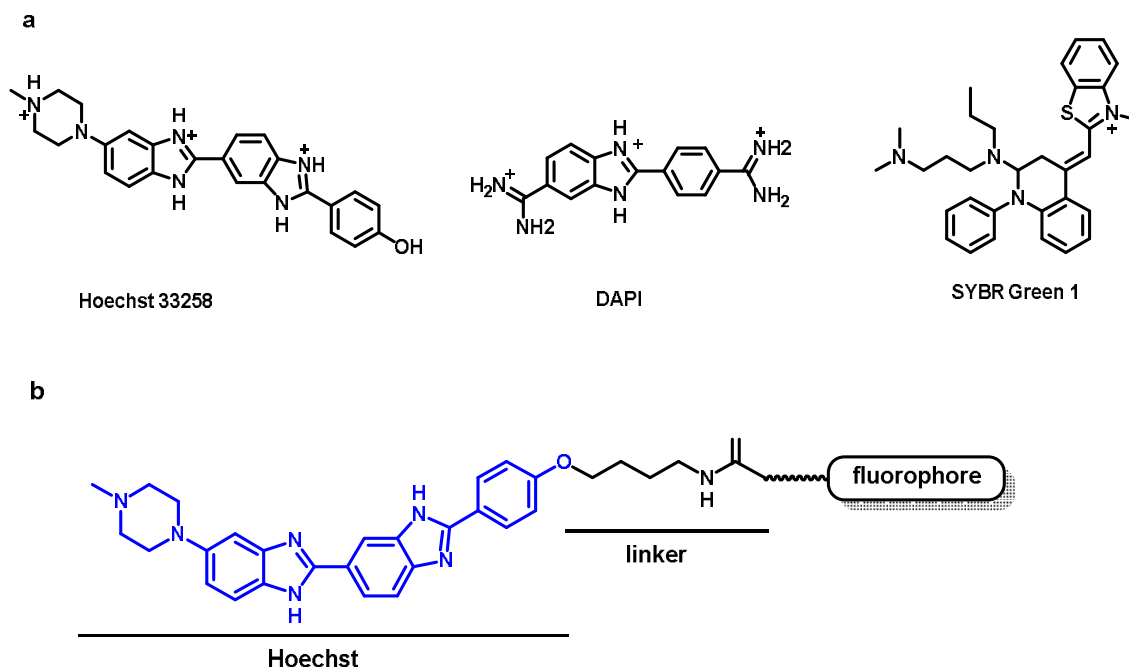


Figure 2. (a) Structures of Hoechst 33258, DAPI and SYBR Green 1. (b) Nucleus-targeted fluorescent probe design strategy based on Hoechst.

2.2. Nuclear Localization Signal (NLS)

The polypeptide with nuclear localization signal (NLS) sequence that can be recognized by the NLS receptor on the nuclear membrane and located in the nuclear region is called the NLS peptide. Another nuclear targeting strategy is to use the NLS short peptides rich in basic amino acids, such as arginine and lysine, which can strongly interact with nuclear pore complexes. Exogenous substances, such as fluorescent probes can also be efficiently introduced into the nucleus by using such amino acid sequences [13]. Figure 3 shows a nuclear localization signal peptide with the amino acid sequence of VQRKRQKLMP. These basic amino acids tend to form positive charges under physiological conditions, such as guanidinium positive ions from arginine. A large number of positive charges are not only conducive to binding with negatively charged DNA, but also can enhance cell penetration of probes. Moreover, there exist several other NLS peptides, such as PKKKRKV, KSRKRKL, RRKRQR, etc.

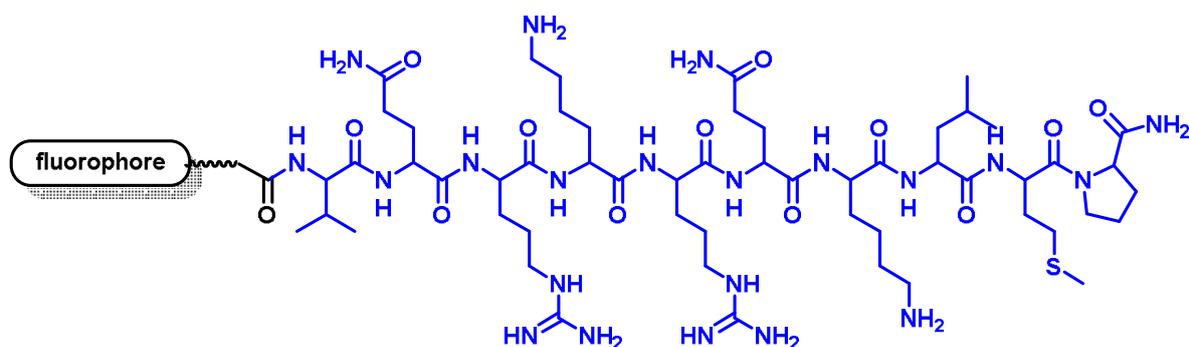


Figure 3. Nucleus-targeted fluorescent probe design strategy based on the NLS group (VQRKRQKLMP).

3. Mechanism of the Nucleus-Targeted Fluorescence Probe into the Nucleus

Most of the currently developed nucleus-targeted fluorescent probes rely on NLS to achieve nucleus penetration. The mechanism of NLS entry into the nucleus has been relatively well studied. Therefore, we introduce the mechanism of nucleus-targeted fluorescent probe linking NLS (NLS-probe) into the nucleus. The transport of the NLS-probe from the cytoplasm to the nucleus is a process mediated by importin proteins. Importin α is an adaptor that links the NLS-probe to importin β . Importin β is a transport factor that carries the NLS-probe through the NPC. Ran is the most abundant member of the small Ras family GTPases, which provide the energy of nuclear transport. Ran, with the assistance of guanine nucleotide exchange factors (RanGEF) and GTPase-activating proteins (RanGAP), acts as a molecular switch that undergoes conformational changes between GDP- and GTP-bound states [14]. The mechanism of the NLS-probe into the nucleus can be divided into three steps: assembly in cytoplasm, translocation through NPC, and disassembly in the nucleus (Figure 4). Step 1: NLS-probe is recognized by the importin α , and subsequently recognized by the importin β to form an NLS-probe-importin α -importin β trimer. Step 2: Importin β can interact with the NPC, allowing the trimeric complex to translocate to the nucleus. Step 3: Once the trimeric complex enters the nucleus, RanGTP binding leads to conformational change of importin β that releases importin β . Then, importin α binds with Nup50 promoting the release of the NLS-probe in the nucleus [15].

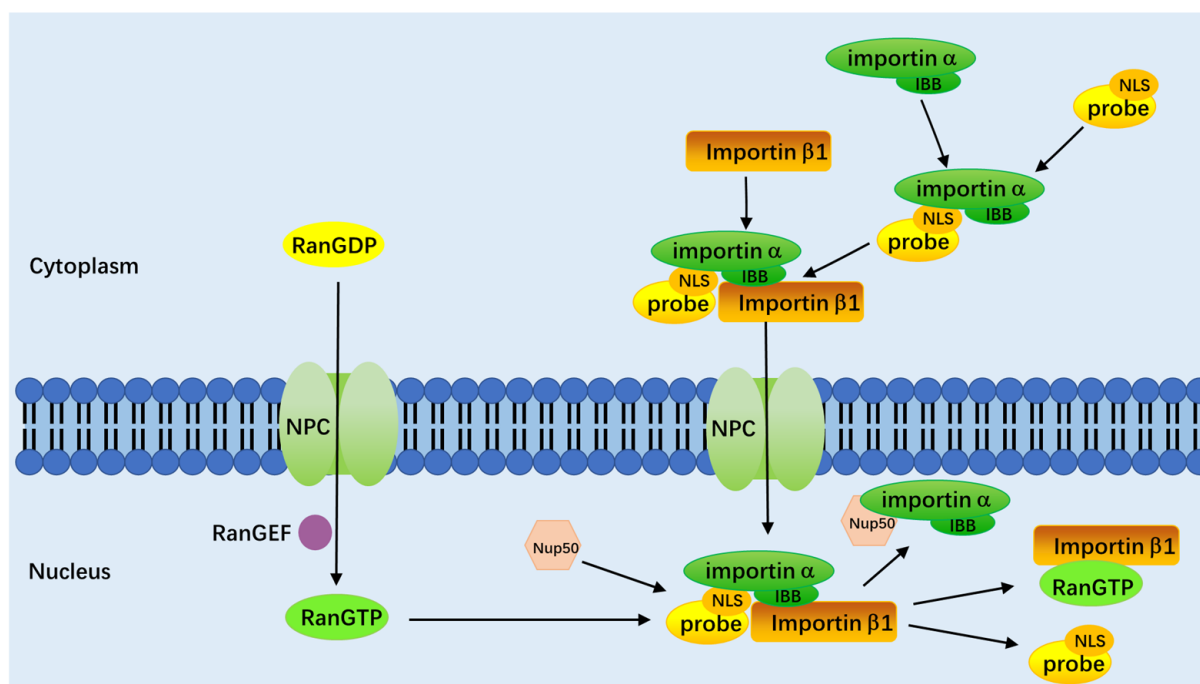


Figure 4. Schematic model of the nucleoplasmic transport of the NLS-probe.

In addition, although there are some other small-molecule fluorescent probes without linking NLS, they still have a good ability for nucleus penetration. However, the mechanism of penetration into the nucleus currently remains unclear. We speculate that there may be the following reasons: 1. Similar to the NLS, these probes also carry a large number of positive charges under a physiological environment, which makes them possible to combine with some nuclear transport proteins to enter the nucleus through NPCs. 2. Small-molecule probes with many positive charges may bind to nucleic acids present in the cytoplasm and then enter the nucleus. 3. As it was reported that soluble small molecules are preferred to diffuse across the nuclear pore, these small-molecule fluorescent probes have a good hydrophilic balance and therefore possess the ability to diffuse across the

nuclear pore. The superior nuclear pore permeability of these small-molecule probes may be due to its good solubility due to the hydrophilic group and shorter alkyl chains.

4. Applications of the Nucleus-Targeted Fluorescent Probes

4.1. Nuclear Imaging

The nucleus is the most complex organelle in the cell, containing substances, such as DNA and RNA, and controls cellular activities by directing protein synthesis. In bioimaging studies, one of the most important tasks is to stain the nuclei of living cells to distinguish organelles. For example, visualization of the nuclei is widely used in studies of cell growth and development [16], fluorescent probe colocalization [17], DNA quantification [18] and cancer biology [19]. In addition, nucleic acid distribution and behavior within the nucleus is a dynamic process, which is closely related to the normal physiological function of the cell. Tracking the dynamic changes of nucleic acids within living cells is of great significance for understanding the dynamic behavior and functional relationship of nucleic acids in different biological processes. For example, the situation of cell division behavior and cell apoptosis could be visually observed using nucleus imaging. Currently, the commonly used nuclear stains mainly fall into two categories: organic dyes and transition metal complexes. Organic dyes, such as the minor groove binding agents DAPI and Hoechst are well-known commercial nuclear dyes, but they require UV light for excitation and may cause severe cell damage if irradiated for prolonged periods [20], in addition to the disadvantages of photobleaching, self-quenching and autofluorescence. SYTO stains are a class of cell permeable dyes that can be excited by visible and near-infrared radiation. Unfortunately, they are not a specific nuclear stain and have an unpublished chemical structure. Although the intracellular anthraquinone dye DRAQ5 displays red fluorescence emission and DNA specific labeling, it is a DNA intercalator that severely perturbs the structure and function of nuclear DNA compared to minor groove binders, such as SYTO17 [21]. Transition metal complexes (such as Ru (II) and Ir (III) complexes) have also been investigated for nuclear imaging, and these complexes usually show yellow or red luminescence with long lifetimes, which can be used for time-resolved luminescence imaging [22–24]. However, these noble metal elements are rare, expensive and unstable for many organisms, and may have a comparative large biotoxicity. Therefore, it remains a major challenge to develop new and more perfect fluorescent probes for nuclear imaging. Currently, imaging of the nucleus and nucleolus is mainly through DNA staining and ribosomal RNA (rRNA) staining, respectively. Some fluorescent probes developed in recent years to image the nucleus and nucleolus are presented below. The characteristic properties of these probes are summarized in Table 1.

In 2013, Tsukiji and coworkers reported that a compound hoeTMP (Figure 5, probe 2) consisting of trimethoprim (TMP) ligand linked to Hoechst via a flexible spacer could efficiently localize in the nucleus of living cells (Figure 6a) [12]. Inspired by this, a general strategy for imaging nuclei via Hoechst labeling was proposed in 2014 by Tsukiji et al. [25]. Specifically, linking a Hoechst label to a fluorochrome of interest through flexible long chains allows the molecule to be synthesized to visualize the nucleus in living cells as a DNA binding fluorescent probe. They first synthesized hoeFL by linking a very classical and versatile organic fluorophore, fluorescein, with a Hoechst label through a flexible chain (Figure 5, probe 1) and observed that hoeFL responded well to DNA. However, due to the anionic nature of fluorescein, the cell membrane penetration ability of the hoeFL probe was relatively poor. To address this point, Shinya Tsukiji et al. newly synthesized hoeAc₂FL (Figure 5, probe 1) using 5-carboxyfluorescein diacetate for live cell imaging. Once treated with hoeAc₂FL (5 mM) for 15 min, obvious fluorescence could be observed in the nucleus of HeLa cells (Figure 6b). However, this probe was easily expelled by the intracellular drug resistance pump, and it produced a lower fluorescence brightness compared with Hoechst 33342. In 2015, Johnsson et al. developed a far red DNA fluorescent probe, SiR-Hoechst, using Hoechst 33342 as a DNA targeting ligand coupled with carboxylated silicon rhodamine (SiR, Figure 5) [26]. In 2018, Lukinavicius et al. [27], in order to better understand

the relationship between Hoechst conjugates and the structure and performance of dyes, carried out an in-depth study on the Hoechst conjugates of tetramethylrhodamine (TMR), two carbopyrroles (580CP and 610CP), German rhodamine (GER), and silicon rhodamine (SiR) (Figure 5, probe 3). Live cell imaging showed that the 5'-regioisomer had better imaging ability of the nucleus and was always brighter than the 6'-regioisomer (Figure 6c). It was found that the major groove binding of the 5'-regioisomer probe is dominated by the minor groove binding of DNA, while derivatives containing the 6'-regioisomer can also interact with the major groove. Molecular docking experiments indicated that binding of the probe to the major groove would darken the fluorescence and binding to the minor groove would enhance the fluorescence (Figure 6d). The far-red excitation and emission spectra of this probe can largely reduce the phototoxicity. Furthermore, in 2019, Xiao and coworkers coupled thiorhodamine (SR) with Hoechst 33342 via click reaction to obtain a DNA fluorescent probe, HoeSR (Figure 5) [28].

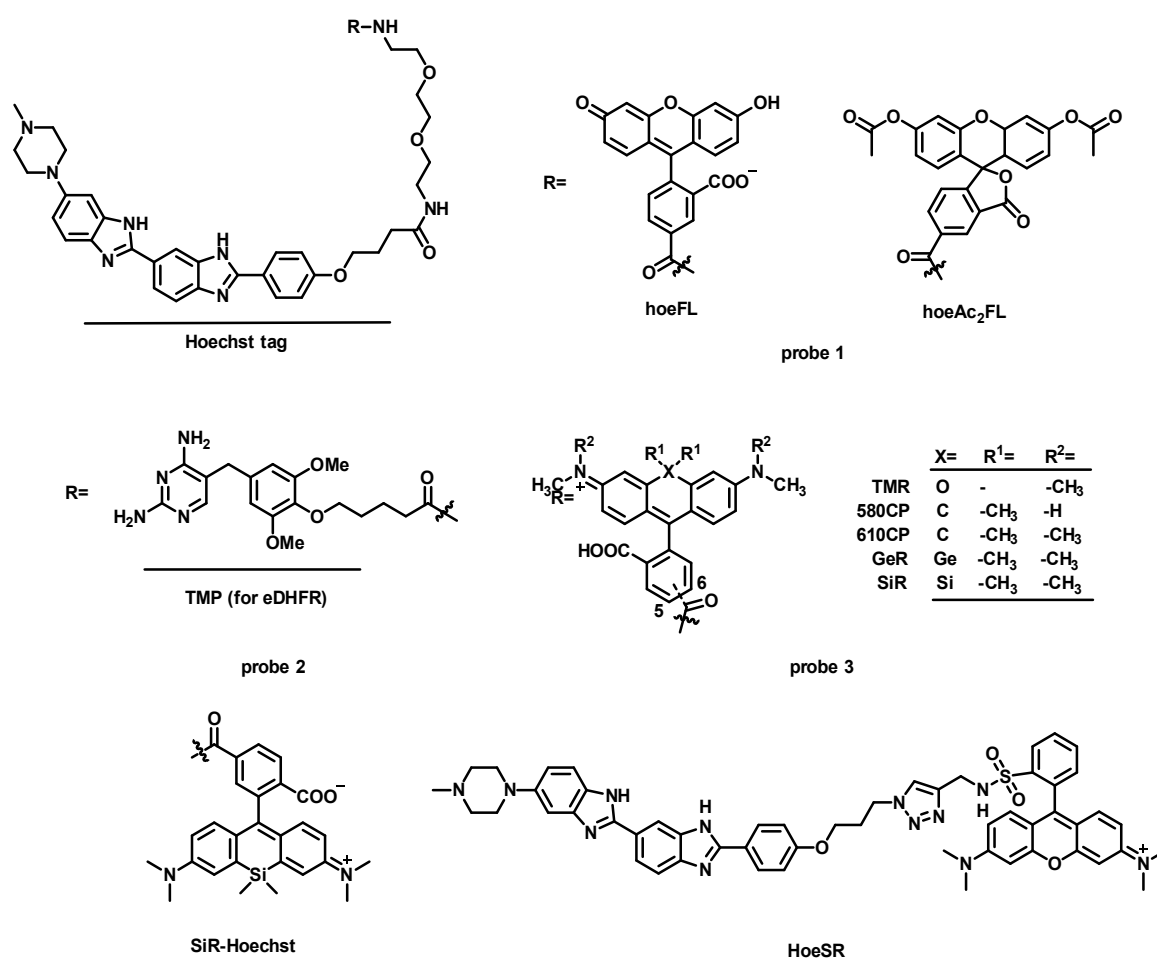


Figure 5. Structures of probe 1, probe 2, probe 3, SiR-Hoechst and HoeSR.

The design of probes to achieve nucleus targeting by ligation of Hoechst is complicated. Structural modification mimicking Hoechst and other classical nucleus dyes is another avenue to obtain nucleus-targeted probes. Peng and coworkers reported a novel red fluorescent dye, DEAB-TO-3, based on TO-3 (a classical RNA dye), which has excitation (626 nm) and emission (649 nm) in the longer wavelength region [29]. DEAB-TO-3 replaced the methyl group of benzothiazole moiety with N, N- diethylaminobutyl group compared to the parent TO-3. Interestingly, DEAB-TO-3 showed better selectivity for AT-rich DNA with an 80.3-fold fluorescence enhancement (Figure 7b). The low fluorescence of the probe (18.9-fold fluorescence enhancement) in the presence of GC-rich DNA is presumably due to photoinduced electron transfer (PET) from the probe to the guanine residue. Live cell

fluorescence imaging of DEAB-TO-3 showed that the probe had a good ability to stain the nucleus (Figure 7e). Moreover, in 2014, Peng and coworkers reported another red fluorescent probe, TO3-CN, developed based on TO-3 dye, which showed good photostability and a large Stokes shift (68 nm) [30]. The photostability of TO-3 was improved by introducing an electron withdrawing group cyano in TO-3, which could inhibit its reactivity with singlet oxygen. In addition, CN groups may interrupt the plane of the molecule and thus decrease the rigidity of the molecular structure, which in turn increases the Stokes shift. The photostability of TO3-CN was tested by sustained irradiation with UV light for 3 h. It can be seen from the Figure 7c that probe TO3-CN still maintained 90% optical density after 3 h irradiation, while TO-3 decreased to around 20%, which illustrated that CN group introduction could indeed increase the photostability. There was a fluorescence response with TO3-CN for both DNA and RNA, but not BSA (Figure 7d). DNA and RNA binding was further demonstrated by deoxyribonuclease (DNase) and ribonuclease (RNase) digestion assays. As shown in Figure 7f, fluorescence from TO3-CN fixation permeabilized MCF7 cells is diminished upon DNase and RNase treatment. The DNA/RNA selectivity of this class of probes needs to be addressed along with determination of binding constants and other characteristic parameters. In addition, Lu et. al. developed a new RNA specific fluorescent probe Styryl-TO [31]. These findings suggest that the styryl group in the structure of styryl plays a key role in RNA specific binding. Cell imaging results showed a strong fluorescence response of Styryl-TO in the nucleolar region (Figure 7g). Compared with DEAB-TO-3 and TO3-CN, Styryl-TO had a shorter excitation wavelength (476 nm) and emission wavelength (535 nm), and was susceptible to the interference of intracellular autofluorescence and was more phototoxic.

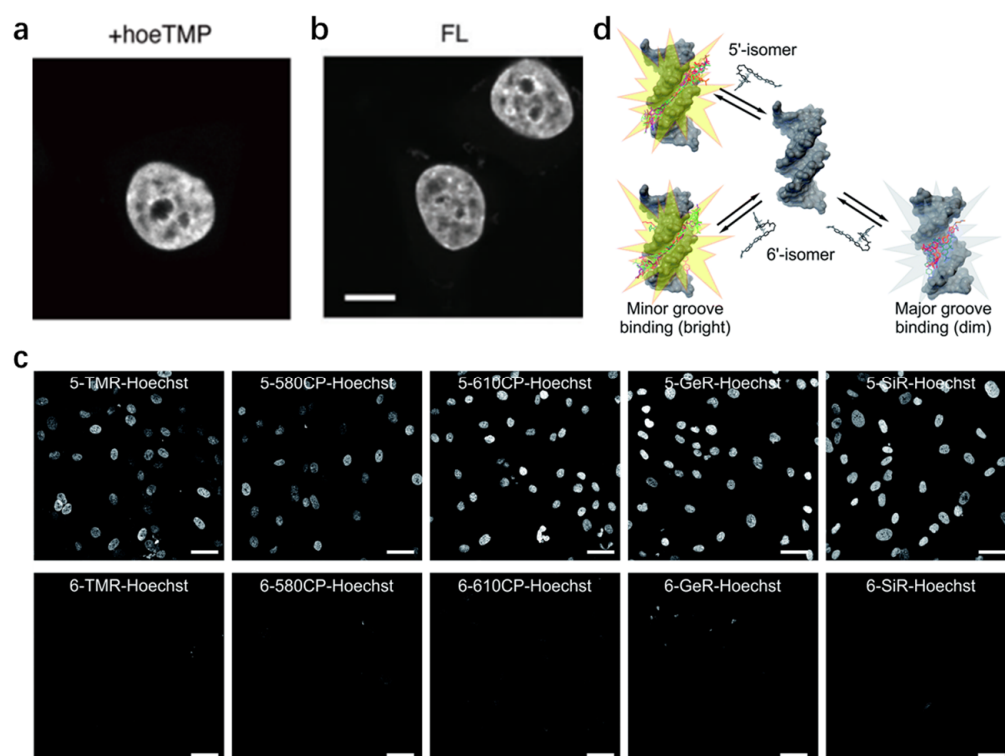


Figure 6. (a,b) Results of cell imaging of hoeTMP and hoeAc₂FL, respectively. Reproduced from [12,25] with permission from the American Chemical Society, Copyright 2013 and Royal Society of Chemistry, Copyright 2014, respectively. (c) Confocal images of 5'-regioisomer and 6'-regioisomer. (d) Proposed model of rhodamine-Hoechst conjugate interaction with the target DNA. Minor groove binding results in a brighter complex compared to major groove binding. Reproduced from [27] with permission from the Royal Society of Chemistry, Copyright 2019.

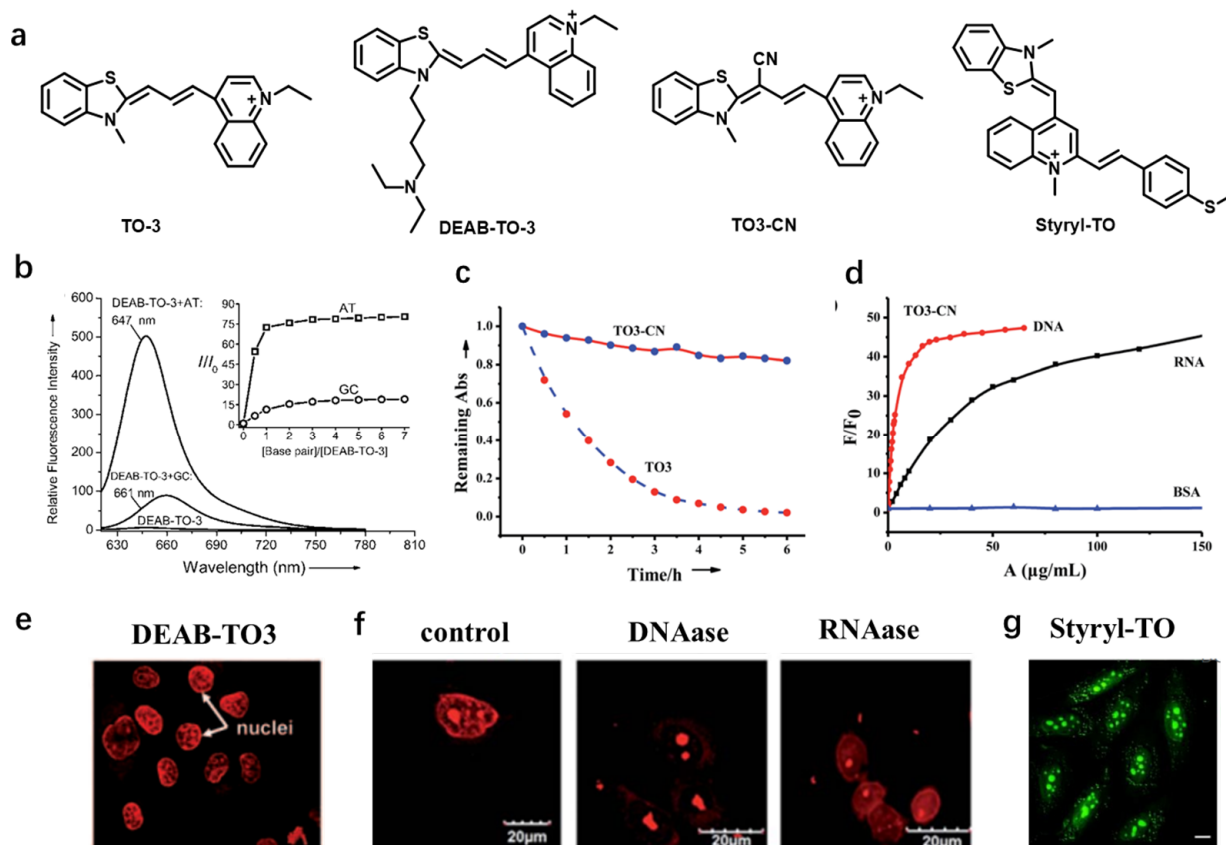


Figure 7. (a) Structures of TO-3, DEAB-TO-3, TO3-CN and Styryl-TO. (b) Fluorescence emission spectra and enhancement of fluorescence intensities during the titration of a solution of DEAB-TO-3 (1 μ M) with poly(dA-dT)₂ and poly(dG-dC)₂ at 20 °C. Inset: The [base pair]/[DEAB-TO-3] molar ratios are from 0.5 to 7. (c) Photostability response of probes TO3-CN. (d) Fluorescence response of TO3-CN (1 mM) to DNA, RNA and bovine serum albumin (BSA). (e) Fluorescence images of DEAB-TO-3 treated live HeLa cells at 5 mM concentration. Reproduced from Ref. [29] with permission from John Wiley and Sons, Copyright 2011. (f) DNase and RNase digest experiments with TO3-CN in MCF7. TO3-CN (excited at 559 nm and collected at 575 nm to 620 nm) was cultured at 2 mM for 45 min. Reproduced from [30] with permission from the Royal Society of Chemistry, Copyright 2014. (g) Fluorescence images of Styryl-TO. Reproduced from [31] with permission from the Royal Society of Chemistry, Copyright 2015.

There are still many cyanine-based probes available for nuclear imaging. Figure 8 illustrates some other monomethylcyanine probes and trimethylcyanine probes developed in recent years. In 2020, a series of CI-TO probes were designed by Kurutos et al. [32]. The anti-photobleaching properties of this series of mono-, di-, and tricationic dyes were improved 5-fold and the cytotoxicity was lower than commercially available thiazole orange. Polyionic monomethylamines exhibit stronger fluorescence enhancement, higher stability constants, and binding constants than the single charged TO analogues. The introduction of multiple positive charges can improve the aqueous solubility, increasing the binding constant between the dye molecule and double-stranded helix (such as CI-TO-5 and CI-TO-6). The UV-vis and fluorescence titration results indicated that CI-TO had a strong binding tendency to DNA. Fluorescence imaging results showed that the CI-TO had staining ability for the nucleus, although they were also present in the cytoplasm. Among them, CI-TO-2 and CI-TO-3 are highly selective for the nucleus. In addition, in 2021, Kurutos and coworkers developed three more monomethyl cyanine probes (AK-C1, AK-C2 and AK-C3) for nucleolar imaging [33]. It was found that they were significantly sensitive to AU-rich RNA (379-fold increase in emission signal). AK-C1, AK-C2 and AK-C3

all stain nucleoli, but their fluorescence is also distributed in the cytoplasm. Fluorescence in the cytoplasm may be the result of their interaction with RNA, mitochondrial DNA, or other macromolecules. In the same year, Aristova et al. also developed three monomethyl cyanine probes (SL-2598, SL-2000, L-29) for nucleolar imaging [34]. All probes were found to be more sensitive to RNA than dsDNA. In particular, SL-2000 and SL-2598 were the most sensitive, exhibiting 400- and 480-fold increases in fluorescence intensity in the presence of RNA, respectively. Fluorescence imaging results indicated that all probes were sensitive to intracellular RNAs, including RNA-rich organelles, nucleoli in the nucleus and RNA in the cytoplasm. Moreover, in 2022, Aristova and coworkers developed an additional symmetric trimethylcyanine probe (T-4) that could be used for nucleolar imaging [35]. T-4 is sensitive to nucleic acids with obvious fluorescence enhancement and also possesses good biocompatibility (~85% cell viability) and photostability, which ensures the applicability of this dye as a potentially useful probe for long-term live cell imaging. We believe that the heavy atoms in the benzoxazole heterocycle decrease the effective length of the π -electron system (i.e., the length of the polymethyl chain), thereby positively affecting the stability of the T-4 probe.

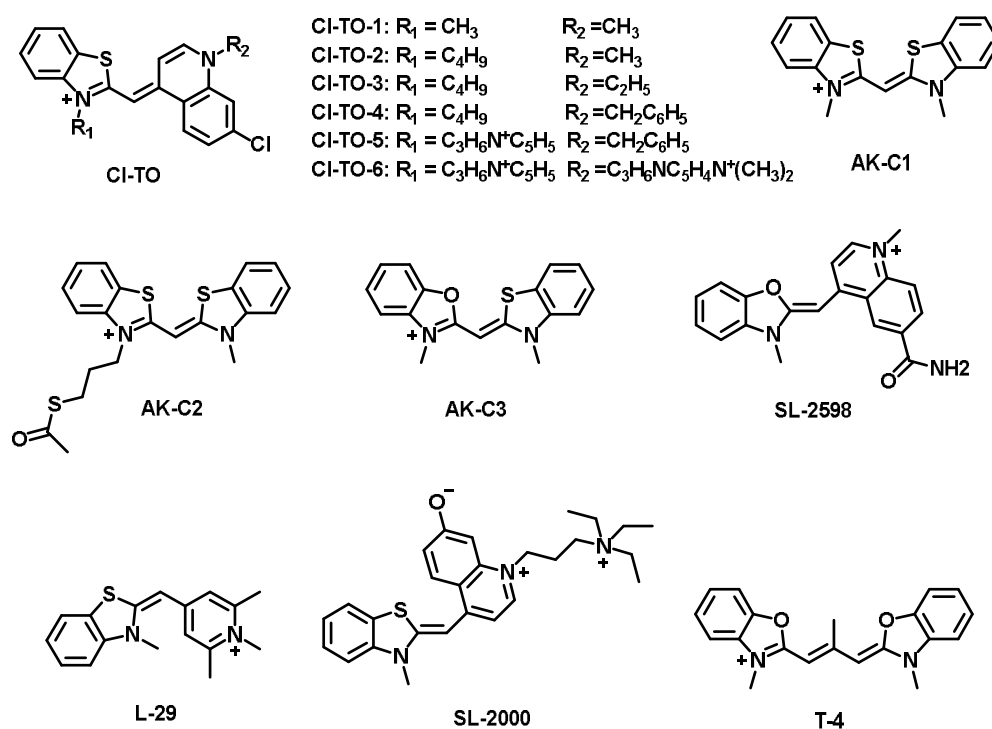


Figure 8. The chemical structures of CI-TO, AK-C1, AK-C2, AK-C3, SL-2598, L-29, SL-2000 and T-4.

Developing targeted fluorescent probes with deep red light into the NIR region (650–950 nm) can effectively avoid the interference of autofluorescence in living organisms, while also improving biological tissue penetration ability as well as reducing phototoxicity in cells and living organisms. Wang and coworkers reported a probe CP with an emission wavelength peak at 658 nm that was used for nucleolar imaging in living cells [36]. In vitro fluorescence studies showed that CP could selectively bound to RNA rather than DNA. The probe exhibited good nucleolar and cytoplasmic staining ability for both normal cells (L929 cells) and cancer cells (A549 cells) (Figure 9b). DNase digestion of cells showed retention of fluorescence intensity, whereas RNase digestion resulted in the complete disappearance of the fluorescence signal of CP in nucleoli (Figure 9c), confirming that the fluorescence enhancement of CP was due to its selective binding to RNA. In addition, CP exhibited superior photostability compared to the commercially available dye SYTO RNaselect. Subsequently, a series of CP family dyes were newly developed by them

through structural modifications [37]. All CP family dyes exhibit absorption maxima in the 584–600 nm region and corresponding emission maxima in the 638–658 nm range. Notably, probes CP3 and CP6, which showed similar staining results with CP in A549 cancer cells as well as normal L929 cells, both clearly stained the nucleoli as well as the cytoplasm of the cells (Figure 9d). However, the RNA selectivity and fluorescence quantum yield of the CP-like probes still need to be further improved.

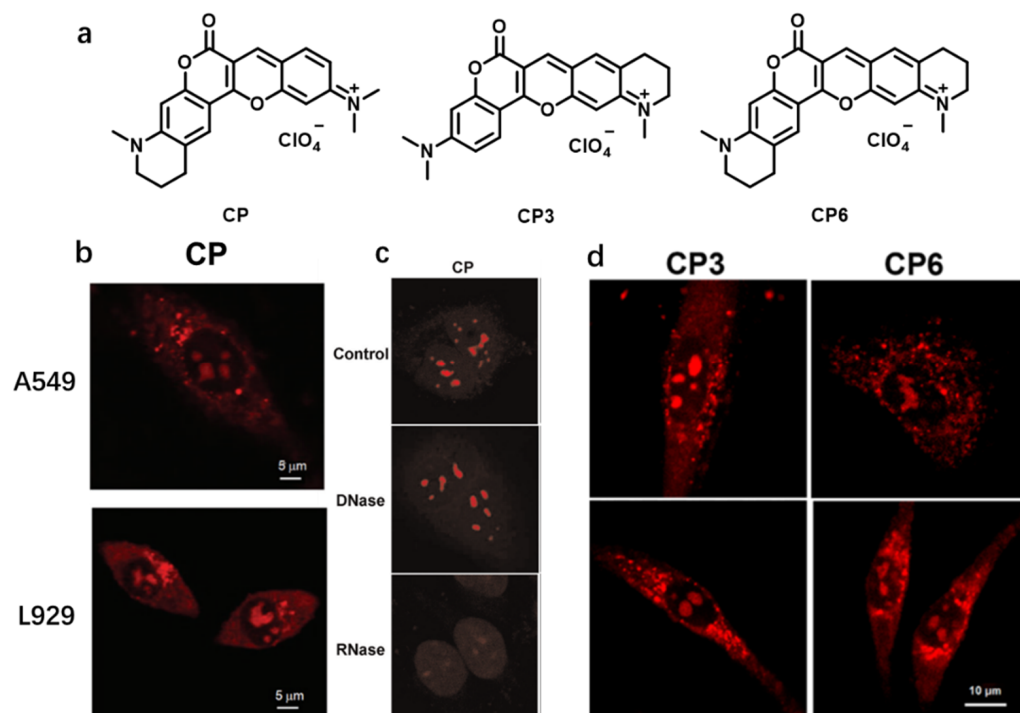


Figure 9. (a) Structures of CP, CP3 and CP6. (b,d) Live cell imaging of A549 and L929 cells with CP, CP3 and CP6. [CP] = 5 μM, [CP3] = 7 μM, and [CP6] = 7 μM. (c) DNase and RNase digest experiments. Reproduced from [36] and [37] with permission from Elsevier, Copyright 2015 and the American Chemical Society, Copyright 2015, respectively.

In recent years, an increasing number of transition metal complexes have been found useful for nuclear imaging. Thomas et al. reported that a dinuclear ruthenium (II) polypyridyl complex ($\lambda_{em(DNA)} = 680$ nm) can be used as a nuclear DNA stain (Figure 10, probe 4) [24]. However, due to its high hydrophilicity and charge, the probe does not enter cells well, requiring a substantial increase in probe concentration. In addition, Barton's group published recognizable mispaired DNA probes 5–6 with ruthenium complexes as DNA recognition groups (both excitation wavelengths were 440 nm) [38,39]. The fluorescence intensity of probe 5 upon binding to mispaired DNA is 26-fold higher than that of correctly paired DNA. Probe 6, which connects sterically bulkier aromatic ligands, exhibits 500-fold higher fluorescence intensity when bound to incorrectly paired DNA than when bound to correctly paired DNA, compared to probe 5. Moreover, they designed a recognizable mispaired DNA probe 7 with rhodium complex as the DNA recognition group [40]. Probe 7 emits a weak fluorescence when free in solution or bound to correctly paired DNA, but a bright fluorescence when a mismatch containing DNA duplex is present. Unlike probes 5 and 6, probe 7 incorporated the cationic indotrimethylcyanine (Cy3) as the fluorescent output group, increasing the excitation wavelength (excitation at 520 nm). However, this class of metal complexes not only faces obstacles on the cellular uptake in living cells and in vivo applications, but also requires extreme care for detailed toxicity studies involving DNA and off-target interactions.

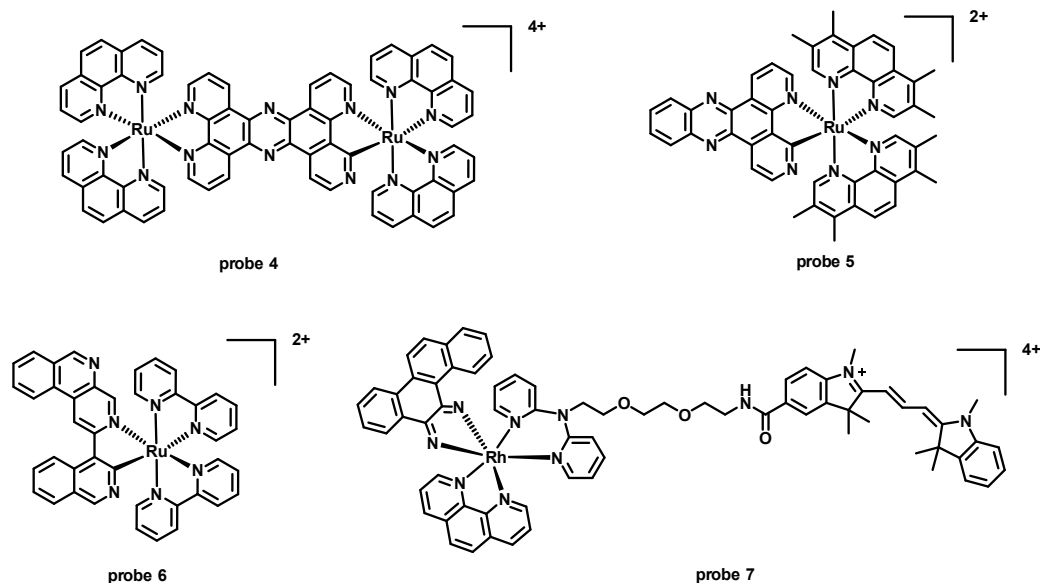


Figure 10. Structures of probe 4–7.

Carbon dots are a new class of fluorescent nanomaterials that have gained increasing popularity over the past decade due to their unique optical properties, good biocompatibility, low toxicity, great aqueous stability, etc. [41,42]. Serdiuk and coworkers developed a fluorescent probe based on SiC nanoparticles [43]. Studies have found that cell division (or proliferation) plays a key role for the cellular uptake and nuclear targeting of probes. Regrettably, the relationship between cell division and SiC NP nuclear uptake is unclear. In 2019, Zhang et al. reported a cationic carbon quantum dot (cQD) probe that binds to dsDNA and ssRNA in living cells in different ways, emitting green and red fluorescence in the nucleus and nucleolus, respectively, and can be used to simultaneously image two types of genetic materials (Figure 11a) [44]. The dsDNA molecules with high structural rigidity confine the cQDs into the grooves, thereby enhancing the fluorescence of the isolated particles, while the flexible ssRNA acts as a cQDs collector, effectively clustering the cQDs so that they emit red fluorescence (Figure 11b,c). In addition, this cQD probe possesses great photostability and biological barrier permeation ability.

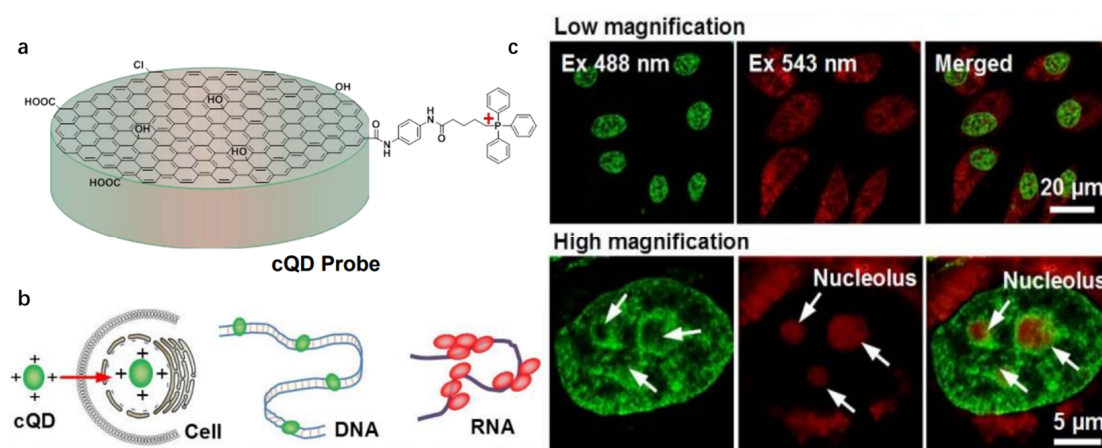


Figure 11. (a) The structure of the cQD probe. (b) Schematic drawing of the cQD probe interactions with intracellular DNA and RNA. cQD confined by dsDNA emits green fluorescence, and cQD clustered by ssRNA emits red fluorescence. (c) cQD-loaded HeLa cells simultaneously excited with 488 and 543 nm (emission windows of 500–560 nm and 570–650 nm, respectively). Reproduced from [44] with permission from John Wiley and Sons, Copyright 2019.

Table 1. Summary of the characteristic properties of the nucleus-targeted fluorescent probes for nuclear imaging.

| Name [Ref.] | λ_{ex} (nm) | λ_{em} (nm) | Stokes Shift (nm) | Binding Constant | Quantum Yield Bound/Unbound | Nucleic Acid Specificity |
|----------------------|---------------------|---------------------------|---------------------------|---|-----------------------------|--------------------------|
| probe 1 [25] | 460 | 520 | 60 | $K_D = 2.5 \times 10^6 \text{ M}^{-1}$ | 0.0072/0.44 (hpDNA) | AT-rich DNA |
| 5-TMR (probe 3) [27] | 558 | 586 | 28 | $K_D = 3.65 \times 10^7 \text{ M}^{-1}$ | ~0.007/0.209 (hpDNA) | AT-rich DNA |
| 6-TMR (probe 3) | 562 | 585 | 23 | $K_{D1} = 1.4 \times 10^8 \text{ M}^{-1};$ $K_{D2} = 1.68 \times 10^8 \text{ M}^{-1}$ | ~0.005/0.052 (hpDNA) | AT-rich DNA |
| 5-580CP (probe 3) | 588 | 613 | 25 | $K_D = 1.55 \times 10^8 \text{ M}^{-1}$ | ~0.027/0.372 (hpDNA) | AT-rich DNA |
| 6-580CP (probe 3) | 594 | 619 | 25 | $K_{D1} = 2.7 \times 10^8 \text{ M}^{-1};$ $K_{D2} = 3.62 \times 10^7 \text{ M}^{-1}$ | ~0.011/0.124 (hpDNA) | AT-rich DNA |
| 5-610CP (probe 3) | 614 | 641 | 27 | $K_D = 3.47 \times 10^7 \text{ M}^{-1}$ | ~0.052/0.432 (hpDNA) | AT-rich DNA |
| 6-610CP (probe 3) | 618 | 644 | 26 | $K_{D1} = 6.5 \times 10^8 \text{ M}^{-1};$ $K_{D2} = 4.4 \times 10^6 \text{ M}^{-1}$ | ~0.033/0.282 (hpDNA) | AT-rich DNA |
| 5-GeR (probe 3) | 641 | 660 | 19 | $K_D = 4.4 \times 10^6 \text{ M}^{-1}$ | ~0.054/0.392 (hpDNA) | AT-rich DNA |
| 6-GeR (probe 3) | 643 | 662 | 19 | $K_D = 5.72 \times 10^7 \text{ M}^{-1};$ | ~0.033/0.207 (hpDNA) | AT-rich DNA |
| 5-SiR (probe 3) | 651 | 672 | 21 | $K_D = 4.8 \times 10^6 \text{ M}^{-1}$ | ~0.007/0.374 (hpDNA) | AT-rich DNA |
| 6-SiR (probe 3) | 654 | 677 | 23 | $K_D = 6.69 \times 10^7 \text{ M}^{-1}$ | ~0.003/0.156 (hpDNA) | AT-rich DNA |
| SiR-Hoechst [26] | 652 | 672 | 20 | $K_D = 8.4 \times 10^6 \text{ M}^{-1}$ | — | DNA |
| HoeSR [28] | 572 | 590 | 18 | $K_D = 3.5 \times 10^6 \text{ M}^{-1}$ | 0.009/0.09 (hpDNA) | DNA |
| DEAB-TO-3 [29] | 626 | 649 | 23 | — | 0.36 | AT-rich DNA |
| TO3-CN [30] | 543 | 604 | 56 (DNA); 49 (RNA) | — | 0.73 (DNA); 0.72 (RNA) | DNA and RNA |
| Styryl-TO [31] | 476 | 535 | 59 | $K_D = 1.23 \times 10^6 \text{ M}^{-1}$ | 0.506/0.0016 | RNA |
| Cl-TO-1 [32] | 508 | 534 | 26 | $K_s = 2.22 \times 10^6 \text{ M}^{-1}$ | — | DNA |
| Cl-TO-2 [32] | 509 | 536 | 27 | $K_s = 2.16 \times 10^6 \text{ M}^{-1}$ | — | DNA |
| Cl-TO-3 [32] | 510 | 536 | 26 | $K_s = 1.26 \times 10^6 \text{ M}^{-1}$ | — | DNA |
| Cl-TO-4 [32] | 513 | 540 | 27 | $K_s = 6.32 \times 10^6 \text{ M}^{-1}$ | — | DNA |
| Cl-TO-5 [32] | 511 | 538 | 27 | $K_s = 4.56 \times 10^6 \text{ M}^{-1}$ | — | DNA |
| Cl-TO-6 [32] | 514 | 539 | 25 | $K_s = 4.76 \times 10^6 \text{ M}^{-1}$ | — | DNA |
| AK-C1 [33] | 421 | 472 | 51 | $K_s = 6.92 \times 10^6 \text{ M}^{-1}$ | 0.0005 (in water) | AU-rich RNA |
| AK-C2 [33] | 422 | 481 | 59 | $K_s = 6.46 \times 10^6 \text{ M}^{-1}$ | 0.0009 (in water) | AU-rich RNA |
| AK-C3 [33] | 400 | 431 | 31 | $K_s = 1.29 \times 10^6 \text{ M}^{-1}$ | 0.0031 (in water) | AU-rich RNA |
| SL-2598 [34] | 504 | 526 | 22 | — | 0.44 | RNA |
| SL-2000 [34] | 506 | 529 | 23 | — | — | RNA |
| L-29 [34] | 451 | 476 | 25 | — | — | RNA |
| T-4 [35] | 499 | 511 | 12 | — | — | RNA |
| CP [36] | 598 | 658 | 60 | — | 0.22 (in DCM) | RNA |
| CP3 [37] | 584 | 638 | 54 | — | 0.555 (in DCM) | RNA and lysosome |
| CP6 [37] | 595 | 655 | 60 | — | 0.338 (in DCM) | RNA and lysosome |
| probe 4 [24] | 450 | 658 (duplex); 631 (GQ) | 208 (duplex); 181 (GQ) | $K_b > 10^5$ (duplex); $4.4 \times 10^6 \text{ M}^{-1}$ (GQ) | — | Duplex and GQ |
| probe 5 [38] | 440 | 660 | 220 | $K_B = 6.8 \times 10^4 \text{ M}^{-1}$ (well-matched DNA); $K_B = 1.8 \times 10^6 \text{ M}^{-1}$ (mismatched DNA) | — | DNA |

Table 1. Cont.

| Name [Ref.] | λ_{ex} (nm) | λ_{em} (nm) | Stokes Shift (nm) | Binding Constant | Quantum Yield Bound/Unbound | Nucleic Acid Specificity |
|----------------|-----------------------------|-----------------------------|-------------------|---|-----------------------------|--------------------------|
| probe 6 [39] | 440 | 700 | 260 | $K_B = 7.3 \times 10^3 \text{ M}^{-1}$ (well-matched DNA); $K_B = 3.5 \times 10^6 \text{ M}^{-1}$ (mismatched DNA) | — | DNA |
| probe 7 [40] | 520 | 570 | 50 | $K_D = 3.2 \times 10^7 \text{ M}^{-1}$ (mismatched DNA) | — | DNA |
| cQD probe [44] | ~400(dsDNA); ~540(ssRNA) | ~520(dsDNA); ~620(ssRNA) | ~120 | — | ~0.080 | dsDNA; ssRNA |

4.2. Detection of Biomolecules in the Nucleus

4.2.1. Detection of DNA

The development of fluorescent probes that can detect DNA is therefore of extraordinary interest for understanding gene mutations and diseases and for developing effective means of diagnosis and therapy. Figure 12 illustrates several fluorescent probes that have been developed in recent years to detect DNA. Probe 8 developed by Feng et al. based on carbazole is a red fluorescent probe that can detect dsDNA [45]. Probe 8 emits a weak fluorescence at 573 nm. However, when the probe binds to DNA, the fluorescence intensity is enhanced 77-fold along with an increase of fluorescence quantum yield from 0.003 to 0.13. Consequently, this probe possesses good properties for detecting DNA. The study demonstrated that probe 8 binds in the minor groove of DNA and was successfully applied to two-photon detection of DNA in HeLa cells. Furthermore, Duan et al. synthesized a series of organic small molecule fluorescent probes for detection of DNA based on a carbazole backbone [46]. Probe 9 possesses a large Stokes shift (201 nm) and low cytotoxicity. Probe 9 showed a 30-fold enhancement in fluorescence intensity upon binding to DNA. Unlike probe 8, probe 9 was distributed in mitochondria in live HeLa cells and mainly in the nucleus in fixed HeLa cells.

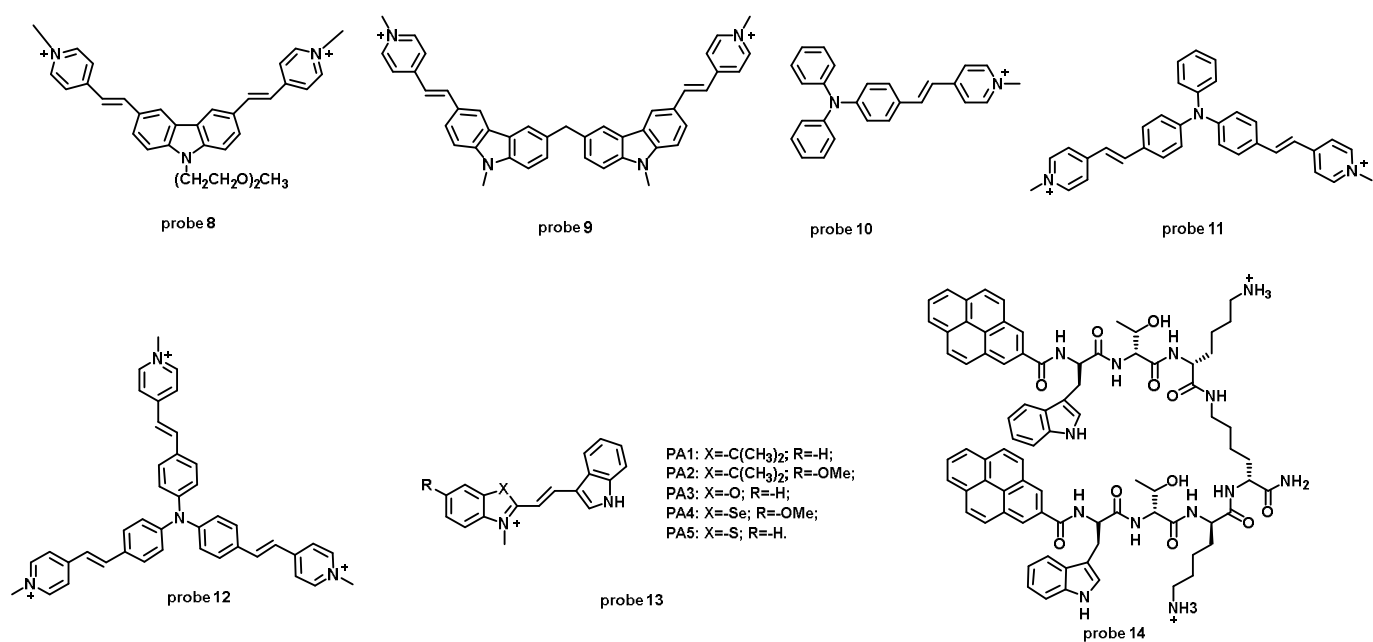


Figure 12. The chemical structures of probe 8–14.

Probes 10–12 were synthesized for detecting DNA using trianiline as a scaffold [47]. Interestingly, these compounds exhibit weak fluorescence in water, while upon binding to dsDNA, their fluorescence emission is strongly recovered (enhancement factors of 20–100). Circular dichroism experiments demonstrate that probes 10–12 bind in the minor groove of DNA. In 2016, Gaur et al. revealed the potential of electron rich heteroatoms of the chalcogen family in improving the binding efficiency and specificity of molecular probes toward DNA, in which the PA5 probe is more capable of intranuclear DNA imaging and detection relative to the probes of PA1–PA4 (PA5 penetrates the cell membrane and stains the nucleus in 15 s) [48]. Moreover, Wu and coworkers developed a pyrene-functionalized cationic oligopeptide probe 14 that can efficiently bind to AT-rich dsDNA [49]. When bound to nucleic acids, probe 14 undergoes a conformational change from a folded to an extended form, thereby converting the fluorescence of probe 14 from excimer emission to monomer emission. Thus, probe 14 functions as a molecular polypeptide beacon for the sensing of different types of polynucleotides, as binding to p(dA-dT)₂ is preferred to GC-rich polynucleotides. In the calculated binding mode, two pyrenes are inserted into the base stack, while the peptide linkers are aligned along the minor groove of the nucleic acid with additional electrostatic interactions between the positively charged lysine side chains and the phosphate backbone. In addition, probe 14 most likely enters the cell by endocytosis and binds to nucleic acids in the nucleus after reaching the nucleus. The imaging results showed that probe 14 produced a strong fluorescence signal in the nucleus and almost no fluorescence was observed in the cytoplasm. Notably, in 2020, the Lin group designed a D- π -A- π -D type of probe QPP-AS by rationally regulating the intramolecular charge transfer (ICT) ability between electron acceptors and electron donors, which could help realize ratiometric fluorescence response to nucleic acids in living cells [50]. As shown in Figure 13b, with the increase of the dsDNA concentration, a new red fluorescence peak appeared at 670 nm for QPP-AS and continuously enhanced, meanwhile the green fluorescence peak at 510 nm remained unchanged. Specifically, after it was intercalated in DNA, QPP-AS molecular movement was restricted, and the hydrophobic environment provided by the nucleic acid matrix could reduce the interaction between QPP-AS and water molecules. These effects reduced nonradiative decay and excitation energy dissipation, thereby causing QPP-AS to produce red fluorescence and exhibit fluorescence gradual enhancement with increasing DNA concentration. QPP-AS showed the capability of living cell imaging at two emission channels ($\lambda_1 = 510 \pm 20$ nm, $\lambda_2 = 670 \pm 20$ nm), in which the red fluorescence channel (670 \pm 20 nm) shows a good nucleus staining. Following DNase treatment, the fluorescence in the nucleus almost disappeared and appeared mainly in the nucleoli and cytoplasm, whereas after RNase treatment, the fluorescence remained in the nucleus. In addition, this probe possesses a good signal-to-noise ratio and can accurately show the distribution location and relative content of nucleic acids in the nucleus (Figure 13c). More importantly, QPP-AS can also monitor the nucleic acid dynamic behavior of different cellular processes, such as nucleic acid distribution for cellular mitotic processes and in situ monitoring of chromatin aggregation and segregation of apoptotic cells.

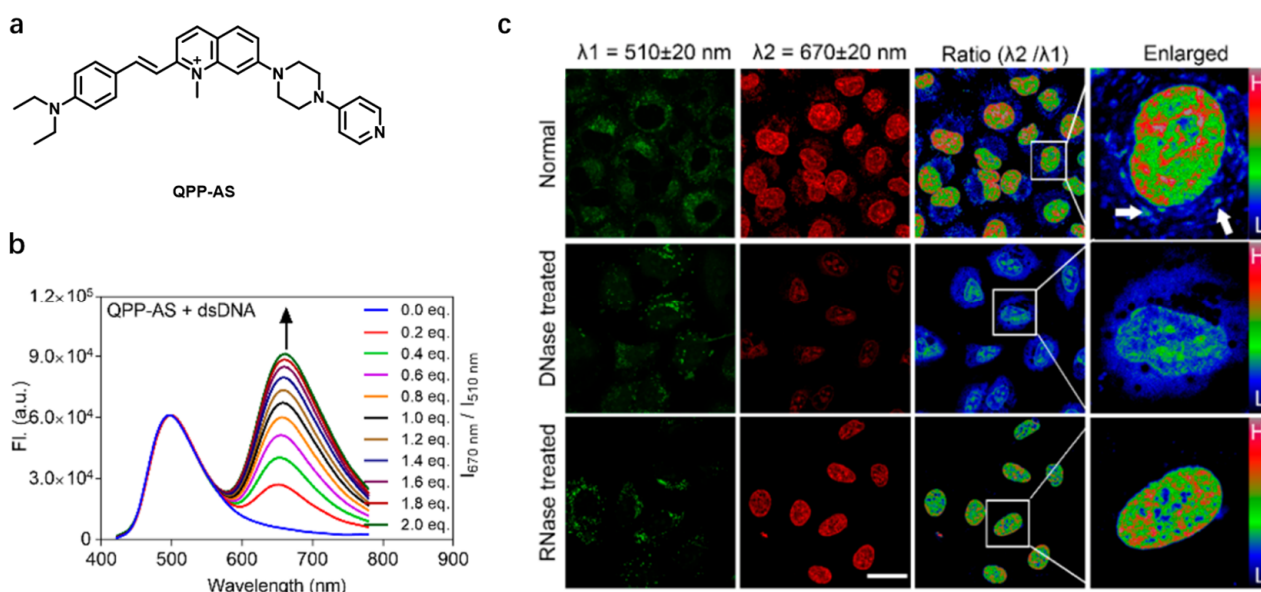


Figure 13. (a) The chemical structure of QPP-AS. (b) Fluorescence response of QPP-AS (3 μ M) to dsDNA in buffer solution. (c) Ratiometric fluorescence imaging of QPP-AS (10 μ M, incubated 2 h) by a dual-emission channel ($\lambda_1 = 510 \pm 20$ nm; $\lambda_2 = 670 \pm 20$ nm; ratio = λ_2/λ_1) at $\lambda_{ex} = 405$ nm in living A549 cells, fixed A549 cells with DNase I (100 U/mL, 2 h) treatment, and RNase A (100 μ g/mL, 2 h) treatment. Reproduced from [50] with permission from the American Chemical Society, Copyright 2021.

4.2.2. Detection of RNA

RNA also plays important roles in cellular physiological processes, such as protein synthesis, gene regulation and reaction catalysis, among others. RNA in the nucleus is concentrated in the nucleolar region, the site of ribosomal RNA (rRNA) transcription, processing and assembly. At present, designing RNA specific fluorescent probes is difficult work because RNAs have flexible conformations of secondary and tertiary structures [51]. In addition, small molecule probes have a stronger binding tendency for DNA than RNA, which also makes the design of RNA specific probes difficult. The only commercially available RNA probe known to date is SYTO RNaselect, a green fluorescent dye (which is easily perturbed by background fluorescence in biological media), but its molecular structure has not been made public to date. Several RNA selective fluorescent probes developed in recent years are presented below (Figure 14). In 2018, Peng and colleagues reported a deep red (705 nm) RNA selective probe NBE based on the Nile scaffold that is more photostable than SYTO RNaselect [52]. However, it is worth noting that SYTO RNaselect exhibits >100-fold fluorescence enhancement upon binding to RNA, compared to 5-fold fluorescence enhancement for NBE, which would result in a lower sensitivity for RNA detection. Nishizawa et al. indicated that this resulted from the lack of a rigid chemical structure of NBE when binding to RNA. In 2019, they developed an RNA fluorescent probe that simultaneously satisfied deep red emission (657 nm) and large fluorescence response (105-fold) based on the asymmetric methylcyanine scaffold benzo [c, d] indole-quinoline monomethine yaninee (BIQ) [53]. In contrast to NBE, BIQ has torsional elasticity around two heterocycles of a central bridge that is key for emitting light signals when bound to RNA. In addition, compared with commercial SYTO RNaselect probes, BIQ offers several advantages, such as high photostability, RNA selectivity, good cell permeability, and negligible cytotoxicity, and can be a candidate fluorescent probe for the imaging analysis of nucleolar RNA.

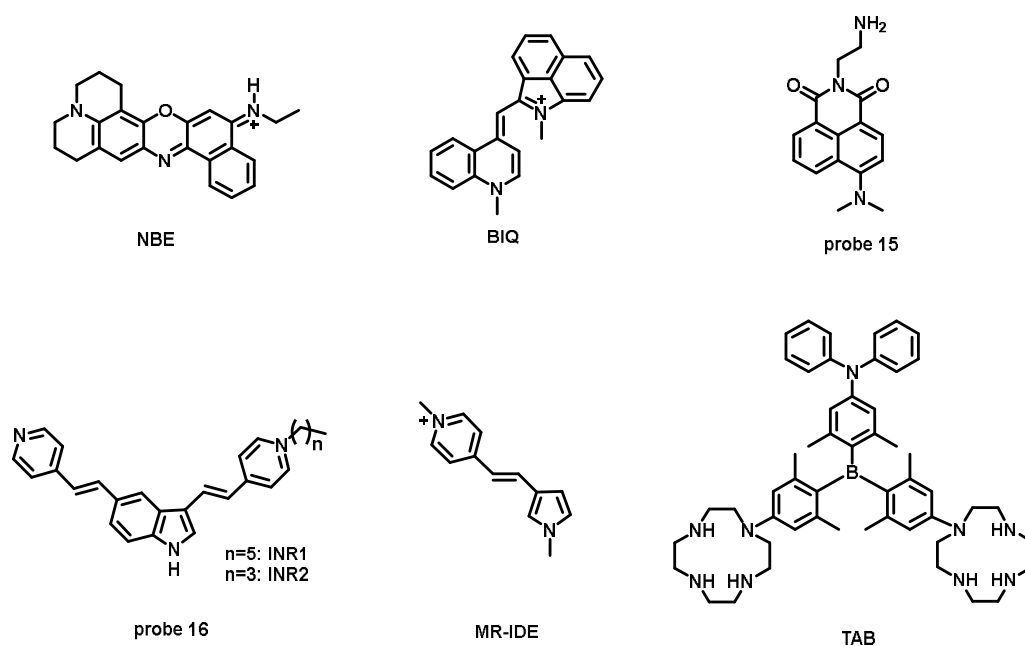


Figure 14. Structures of fluorescent probes for RNA detection.

In 2019, Yi et al. developed a fluorescent probe capable of specifically recognizing ribosomal RNA (rRNA) based on a naphthalimide scaffold [54]. The dimethylamine in the structure of probe 15 could not only serve as a donor for intramolecular charge transfer (ICT), but also decrease the fluorescence quantum yield of the free probe by rotation. In addition, the alkylamine group at the end of this probe acts as a hydrophilic group, which keeps the probe in a hydrophobic balance, thereby increasing the membrane permeability of the probe. *In vitro* studies have shown that probe 15 has a concentration dependent and specific recognition of rRNA (Figure 15a,b). The results of molecular docking and ^1H NMR titration studies indicated that the higher fluorescence enhancement of probe 15 with rRNA was mainly due to the specific binding of probe 15 to the complex 3D structure of rRNA. The live cell fluorescence imaging results indicated that probe 15 could stain rRNA quickly, and obvious green fluorescence could be observed at the nucleolus within 30 s, and the fluorescence intensity reached saturation within 1 min (Figure 15c). Probe 15 exhibits excellent selectivity, remarkable photostability, biocompatibility and excellent cell permeability, and may provide an alternative tool for commercial rRNA staining. In addition, Lin and coworkers developed a fluorescent probe MR-IDE capable of detecting mitochondrial RNA (mtRNA) [55]. However, MR-IDE is detected by insertion into an RNA groove structure, which is susceptible to interference from DNA that also possesses a groove structure, as well as other kinds of RNA. The imaging results of MR-IDE in cancer cells showed that, in addition to the green fluorescence appearing in the cytoplasm, it also presented obvious green fluorescence on the nucleolus due to rRNA interference in the nucleolus. Sun et al. designed and synthesized two low-molecular-weight indolyl mono-cationic probes (probe 16, INR1 and INR2) that were identified as RNA selective fluorescence turn-on probes [56]. These two probes, with good membrane permeability, have been successfully used to image ribonucleic acids in the nucleus and cytoplasm of living cells by confocal and two-photon fluorescence microscopy. Finally, to be introduced is a water-soluble RNA fluorescent probe, TAB, developed by Yang et al., consists of triarylboron, diphenylamine and 1,4,7,10-tetraazacyclododecane (Cyclen) moieties [57]. Conjugated triarylboronic compounds containing electron donating groups are characterized by ICT and exhibit many good fluorescence properties, such as excellent membrane permeability and high quantum yield. The hydrophobic diphenylamine was used to tune the hydrophilicity of the probe, ensuring good cell permeability. Cyclen is frequently used as a scaffold for artificial RNA lyases and shows specificity for RNA, so it serves as an RNA recognition group. Notably,

multiple polar hydrogens in the circularized structure can readily form hydrogen bonds with exposed bases of single stranded RNA, but not with double stranded DNA. In double stranded DNA, strand-strand base pairing prevents these sites from circularizing. Thus, TAB is able to preferentially bind RNA with excellent selectivity. In summary, the design of RNA selective probes is difficult, and the currently available probes for detecting RNA are still very few.

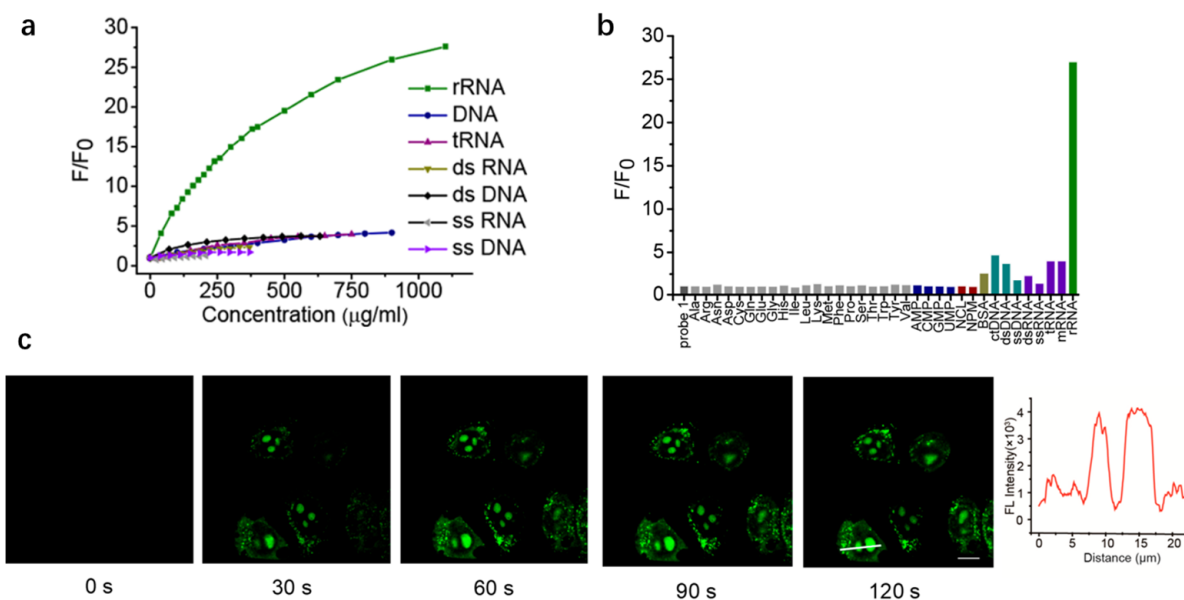


Figure 15. (a) Fluorescent titration of probe 15 at 10 μM with the addition of rRNA. (b) Selectivity of probe 15 (10 μM) versus different species including 20 kinds of amino acids (200 μM), four kinds of mononucleotide acid (200 μM), two nucleolus proteins nucleolin (NCL) (10 μM), and nucleophosmin (NPM) (10 μM), BSA (200 μM), ctDNA (1200 $\mu\text{g/mL}$), synthesized dsDNA (630 $\mu\text{g/mL}$), synthesized ssDNA (370 $\mu\text{g/mL}$), synthesized dsRNA (370 $\mu\text{g/mL}$), synthesized ssRNA (206 $\mu\text{g/mL}$), tRNA (750 $\mu\text{g/mL}$), mRNA (100 $\mu\text{g/mL}$) and rRNA (1000 $\mu\text{g/mL}$) in 20 mM PB at pH 7.2. (c) Time-dependence (0 s, 30 s, 60 s, 90 s, 120 s) CLSM images of HeLa cells incubated with probe 15 at 5 μM ($\lambda_{\text{ex}} = 488 \text{ nm}$, $\lambda_{\text{em}} = 515\text{--}565 \text{ nm}$). Bottom right: fluorescence intensity profile of selected area labeled with a white bar. Scale bar: 10 μm . Reproduced from [54] with permission from the American Chemical Society, Copyright 2019.

4.2.3. Detection of the G-Quadruplex

Usually, DNA exists mainly as a double helix, but some unique structures, such as G-quadruplex also occur. G-quadruplex is a four stranded structure of guanine rich nucleic acid sequences, which can be further divided into three structures, parallel, anti-parallel and hybrid. Notably, G-quadruplex often occurs at telomeres and the promoter regions of certain cancer genes and is thought to be closely associated with aging and disease. Therefore, G-quadruplex has been considered as a potential drug target, and studies based on G-quadruplex have also received increasing attention in recent years. Thiazole orange (TO), a versatile and widely used fluorescent dye for nucleic acids, cannot distinguish G-quadruplex DNA from other DNA species despite its high fluorescence quantum yield. In 2016, Lu and coworkers designed a series of new fluorescent dyes 4a, 4b, 4c, 4d by introducing various styrene substituents on the framework of TO (Figure 16a) [58]. It was found that these newly designed fluorescent dyes were able to bind to nucleic acids and exhibited excellent fluorescence discrimination ability against the G-quadruplex (Figure 16b), among which 4a exhibited the best recognition ability. More importantly, the excellent fluorescence signal discrimination ability was found to be determined by the spatial length and orientation of small substituents of TO molecules. As shown in Figure 16c, 4a can stain the nucleolus region because there are rRNAs within the nucleolus for transcription,

and guanine rich rRNAs may form quadruple conformations. Furthermore, the possibility of 4a binding to RNA in the nucleolus was excluded by RNAase treatment (Figure 16c). Therefore, the newly designed dyes can be used not only for G-quadruplex detection, but also for live cell staining and imaging.

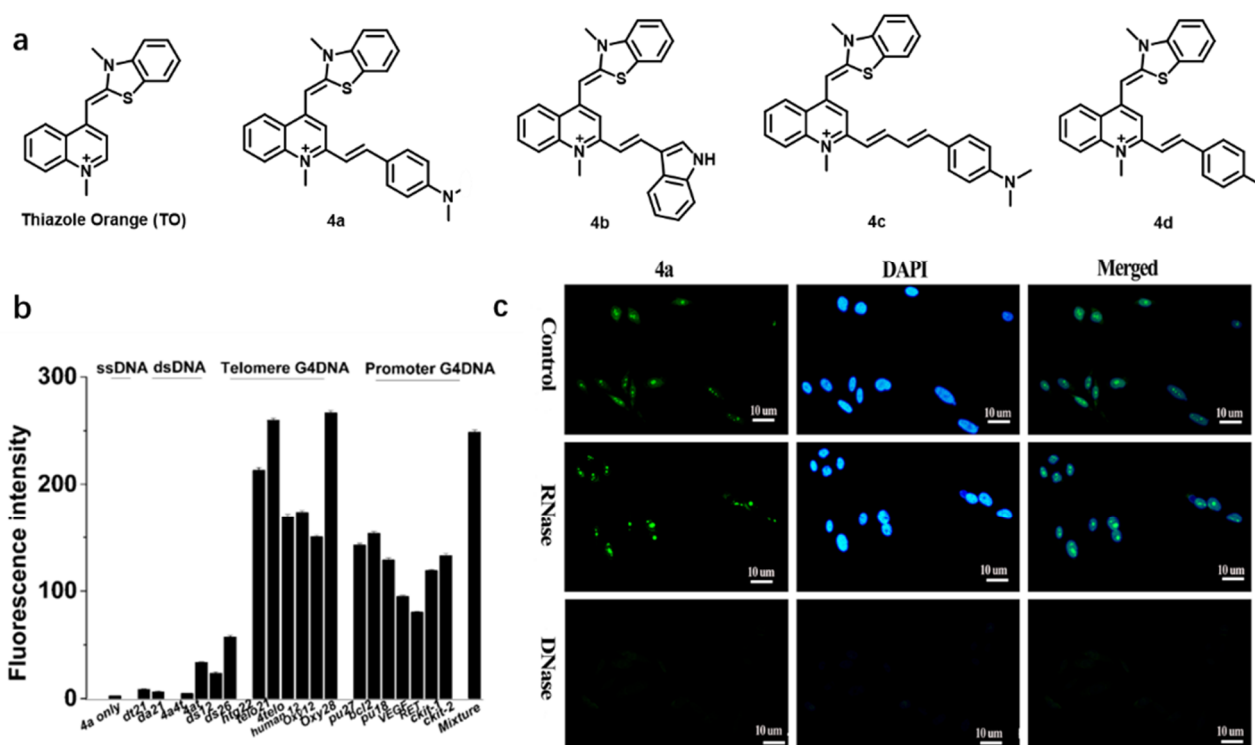


Figure 16. (a) Structures of TO, 4a, 4b, 4c and 4d. (b) Fluorescence intensities at 630 nm ($\lambda_{ex} = 475$ nm) of 4a with different nucleic acids in Tris-HCl buffer containing 60 mM KCl. Single-stranded DNA: da21, dt21. Duplex DNA: 4a4t, 4at, ds12 and ds26. Telomere G-quadruplex DNA: htg22, telo21, 4telo, human 12, oxy12 and oxy28. Promoter G-quadruplex DNA: bcl2, ckit-1, ckit-2, Pu27, Pu18, RET and VEGF. (c) Fluorescence images of PC3 cells (fixed) stained with 5.0 μ M of 4a for 15 min and 1.0 μ g/mL DAPI for 5 min without and with DNase or RNase treatment. 1000 \times magnification was utilized in the imaging. Scale bar is 10 μ m. Reproduced from [58] with permission from the Royal Society of Chemistry, Copyright 2014.

In 2017, Würthner's team developed a G-quadruplex-specific fluorescent probe Dicyanovinyl squaraine dye (SQgI, Figure 17) based on thiazole [59]. The squaraine acid can form an unconventional sandwich π -complex combining two quadruplexes, which results in a strong fluorescence ($\phi_F = 0.61$) supramolecular structure. SQgI exhibits better G-quadruplex selectivity with excitation at 661 nm and emission at 700 nm by one photon absorption in the complexed state. However, this probe still has some deficiencies, including general solubility properties, moderate binding constants and excitation wavelengths outside the biological transparency window (BTWs, NIR-I: 700–950 nm and NIR-II: 1000–1350 nm). In 2018, they developed a water-soluble near-infrared (NIR) amphiphilic squaraine dye (CAS-C1, Figure 17) by modifying dicyanovinyl squaraine moieties by changing to better water-soluble groups that can be used to detect parallel G-quadruplex motifs [60]. The complex of CAS-C1 with parallel G-quadruplex exhibits strong two-photon absorption, which is well suited for NIR to the NIR imaging process. Compared with the previously designed SQgI, CAS-C1 contains a large amount of ethylene glycol chains that can generate strong electrostatic interactions with the G-quadruplex polar backbone to enhance its binding with the G-quadruplex. In addition, a large number of ethylene glycol chains may enhance the affinity of binding to the G-quadruplex by replacing wa-

ter molecules in the groove structure. In summary, the variety of probes able to detect G-quadruplex is still few at present, the recognition mechanism is relatively single, and the selectivity and sensitivity of the probes are still to be improved. Moreover, DNA has multiple substructures (e.g., triplex) in addition to G-quadruplex, which do not appear to be specifically detectable by probes.

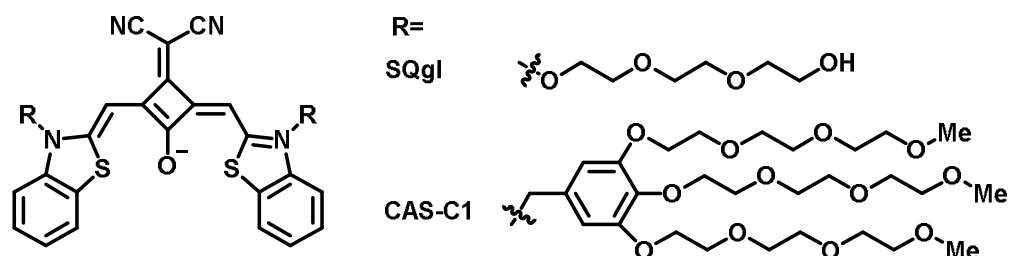


Figure 17. Structures of SQgl and CAS-C1.

4.2.4. Detection of DNA Conformational Changes

Change of DNA conformation is also a key mechanism of gene regulation in organisms during development and disease. Small aberrations in DNA structure could lead to the development of many genetic diseases, such as Friedreich's ataxia (FRDA), Huntington's disease, and myotonic dystrophy [61,62]. Although it is currently possible to characterize DNA structural conformational changes by single-crystal X-ray diffraction, AFM, and cryogenic transmission electron microscopy, these techniques require complex sample processing and only capture the static conformation of DNA, making real-time measurements of transient conformational changes in DNA challenging [63,64]. Li's team developed a fluorescent probe to detect transient DNA conformational changes in DNA structures of different lengths and shapes using the DNA intercalator K21 [65]. K21 can exhibit two forms in a DNA double helical structure: one is a monomer and the other is a dimeric molecule or excimer, both of which exhibit different fluorescence emission spectra. The transient conformational changes produced during DNA respiration may lead to the transition of K21 in monomeric and dimeric (or excimer) forms, resulting in the alteration of the fluorescence emission ratio (Figure 18). K21 has also been successfully applied to identify DNA structures with different transient conformational stabilities, such as mismatched dsDNA, G-quadruplex, i-motifs and single plasmid DNAs with different topologies. In a word, this intercalative fluorescent dimeric probe capable of probing transient conformational changes in DNA would have great potential in nucleic acid analysis applications, but few such probes have been developed.

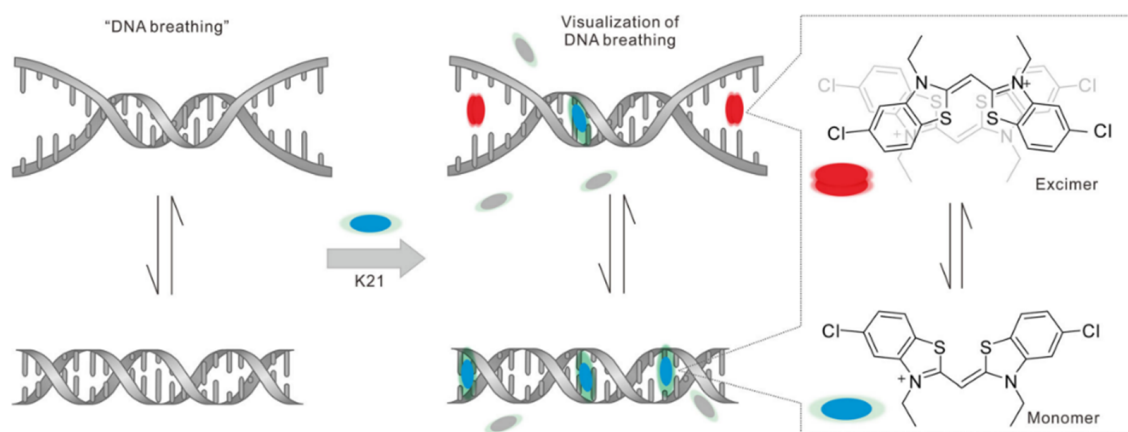


Figure 18. Illustration of proposed binding mechanism between K21 dye and dsDNA. Reproduced from [65] with permission from John Wiley and Sons, Copyright 2021.

4.2.5. Detection of Biological Macromolecules—Histones H2B and HDACs

Histones are DNA bound basic proteins present within chromosomes. Histones are rich in the positively charged basic amino acids arginine and lysine, which can tightly bind to acidic and negatively charged DNA. Histones comprise five components, termed H1, H3, H2A, H2B and H4, in order of molecular weight from large to small. Xiao's team developed a new dye, Rh-Gly, by extending the opening time of the photochromic rhodamine spirolactam, which can be used for the detection and super-resolution imaging of histone H2B in chromosomes inside the nucleus [66]. Rhodamine spirolactams will undergo a reversible structural transition from a nonfluorescent colorless state to a highly fluorescent zwitterion upon UV light irradiation, and such a reversible turn-on switch can avoid the release of additional toxic species. However, achieving super-resolution imaging of histone H2B that provides only strong fluorescence brightness is not sufficient, and it also requires extending the fluorescence emission time of zwitterions. Notably, an acidic environment can be used to stabilize zwitterionic structures. To this end, they added a carboxyl group near the lactam site to provide an intramolecular acidic environment to the rhodamine spirolactam as a way to prolong the opening time of the photogenerated rhodamine spirolactam zwitterion (Figure 19a). Subsequently, by HaloTag fusion protein technology, a chloroalkane ligand conjugated derivative of Rh-Gly (Rh-Gly-Halo, Figure 19b) was prepared. Super resolution imaging of histone H2B, as shown in Figure 19c, the average number of photons per frame of a single molecule was 1040, with an average localization accuracy of 21 nm.

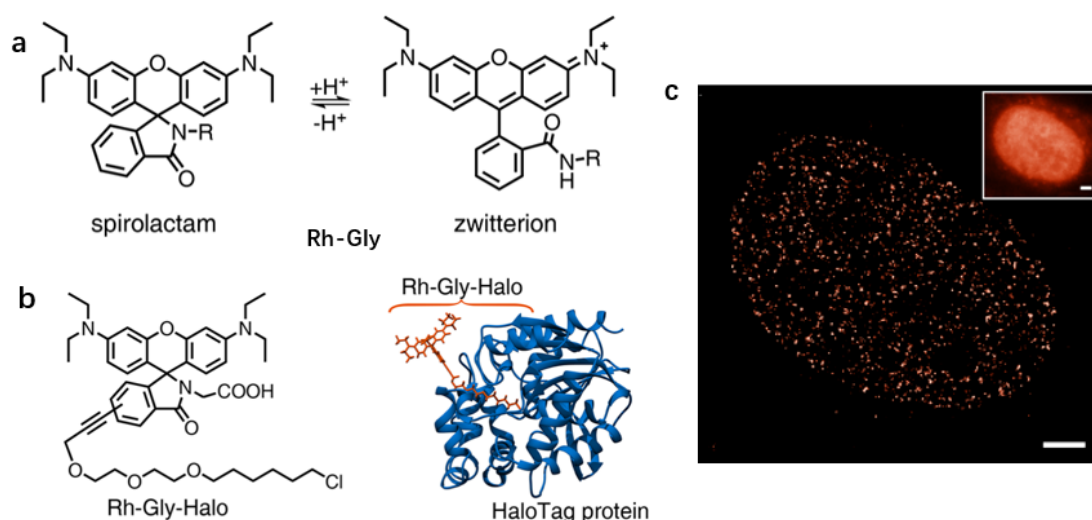


Figure 19. (a) Spontaneous spirocyclization equilibrium of rhodamine spirolactam. (b) Left: molecular structure of Rh-Gly-Halo; right: model of HaloTag protein covalently bounded to Rh-Gly-Halo. Image of Rh-Gly-Halo coupled haloalkane dehalogenase (1BN6) is designed with Chimera. (c) PALM image of H2B-Halo fusion proteins labeled with Rh-Gly-Halo in a live HeLa cell under inclined illumination. Inset shows the wide-field image of the same H2B-Halo fusion proteins labeled with Rh-Gly-Halo. Reproduced from [66] with permission from the American Chemical Society, Copyright 2019.

Histones in the nucleus play an important role for the regulation of chromatin structure and gene expression. However, aberrant downregulation of some genes by histone deacetylases (HDACs) has been found to contribute to several diseases, such as cancer and psychiatric disorders [67]. Therefore, the development of a fluorescent probe capable of detecting the activity of intranuclear HDACs is of high medical value for the diagnosis of diseases. Kikuchi et al., for example, developed a fluorescent probe BOXTO-GK(Ac)G that can detect HDAC activity (Figure 20a) [68]. When the probe has not been deacetylated by HDACs, the interaction between DNA and the probe is weak, and the probe shows little fluorescence, even in the presence of DNA. However, once the probe is deacetylated by

HDACs (BOXTO-GKG, Figure 20a), its charge state becomes more positive, which allows enhanced electrostatic interactions with negatively charged DNA, exhibiting increased fluorescence signal (Figure 20b). Based on this principle, a simple, rapid and continuous detection of HDACs is achieved. Additionally, Rooker's team developed a ratiometric fluorescent probe based on coumarin that could be used to detect HDACs (Figure 20c) [69]. Based on a novel application of the intramolecular imine formation process with amine reactive coumarin fluorophores, probe 17 enables one-step detection of HDACs activity with simple spectrophotometric and fluorescence measurements. It is worth mentioning that, in addition to histones, there are many other kinds of proteins (including enzymes) in the nucleus, and their imaging and detection are still difficult.

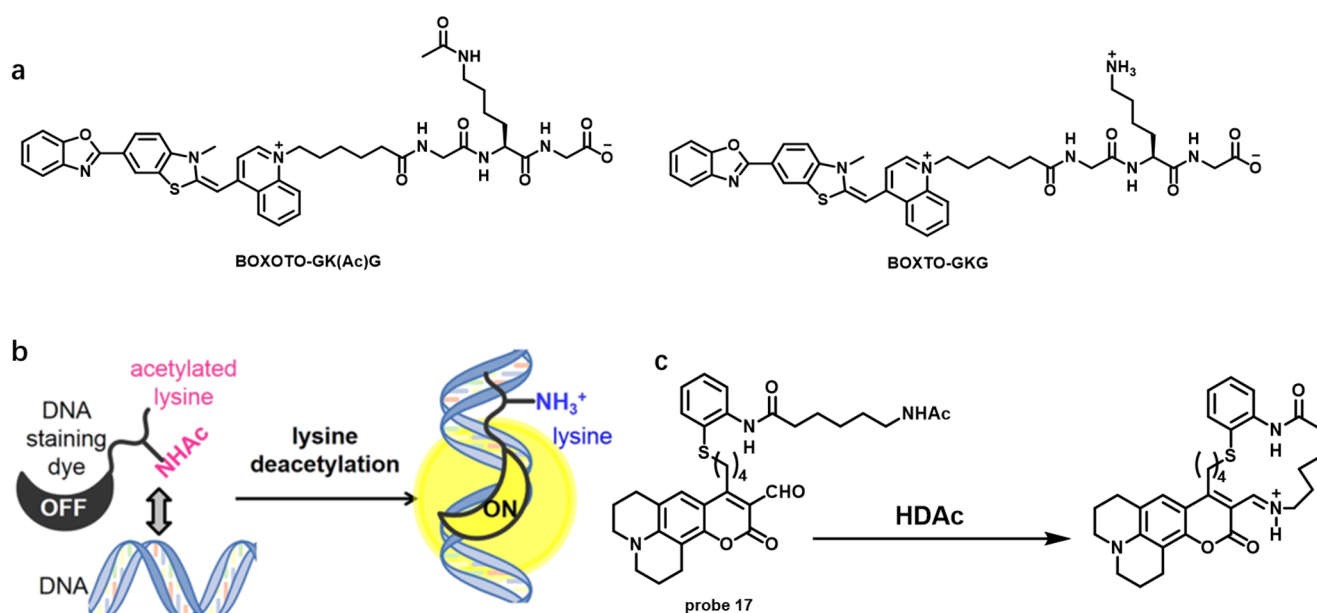


Figure 20. (a) Structures of BOXOTO-GK(Ac)G and BOXTO-GKG. (b) Schematic illustration of the HDAC detection system that uses a fluorogenic probe based on a DNA staining dye. Reproduced from [68] with permission from the American Chemical Society, Copyright 2014. (c) Schematic representation of probe 17 used to detect HDACs.

4.2.6. Detection of Small Molecules and Ions

a. Detection of Pyrophosphate (PPi)

The pyrophosphate (PPi) anion has received increasing attention because of its important role in cellular metabolic processes, such as ATP hydrolysis, and in several diseases, such as calcium pyrophosphate dihydrate crystal deposition disease. However, pyrophosphate has a high solvation energy in water, so it is relatively difficult to design fluorescent probes for detecting PPi with a low detection limit (nanomolar scale) under physiological conditions. In addition, PPi has a strong coordination affinity with metal ions. Inspired by this, Chao and coworkers developed a tripyridine zinc (II) complex, CZtpyZn, for the detection of pyrophosphate based on aggregation-induced-emission (AIE) and ICT [70]. Strong fluorescence emission was observed when CZtpyZn PPi aggregated into nanoaggregates, which could effectively suppress the quenching effect caused by polar solvents, such as water (Figure 21a). As shown in Figure 21b,c, CZtpyZn is highly selective for PPi, whereas it responds poorly to ATP, ADP, AMP and other anions. Importantly, it is worth noting that the probe can also be used for staining the nucleus of living cells (Figure 21d).

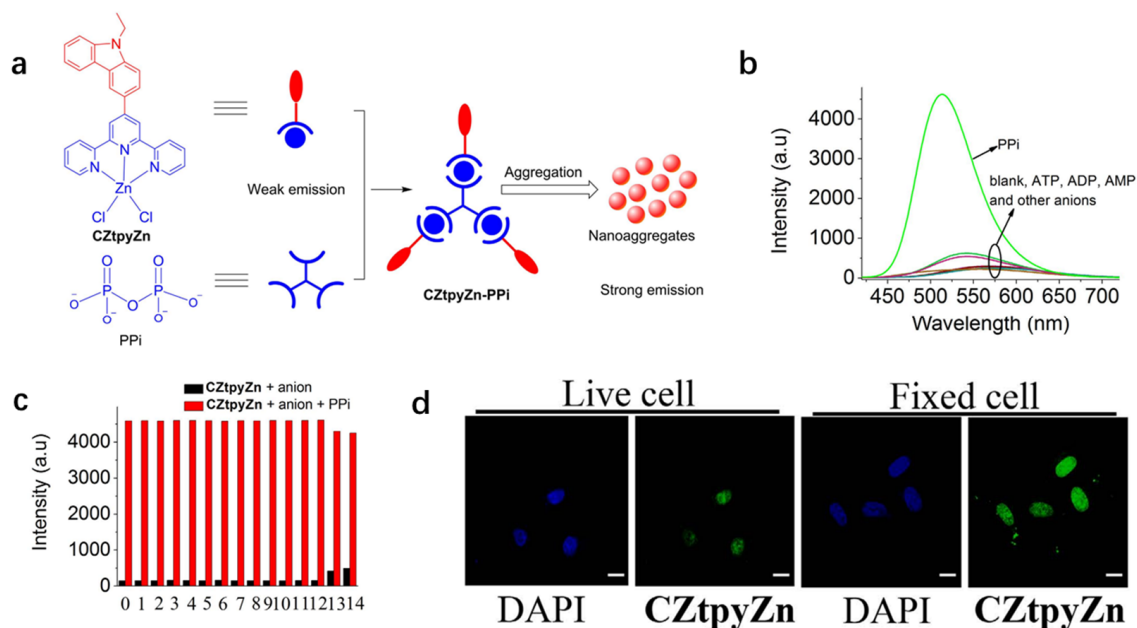


Figure 21. (a) Proposed strategy for the detection of PPI in water medium. (b) Fluorescence spectra of CZtpyZn (10 μM) in the presence of anions (4 μM for PPI and 30 μM for other anions) when excited at 400 nm in HEPES buffer (pH = 7.4, 10 mM in H₂O/DMSO, 7/3, v/v) at room temperature. (c) Fluorescence responses (515 nm) of CZtpyZn (10 μM) to various anions (30 μM) without PPI (black bar) and with PPI (4 μM, red bar) (namely 0–blank, 1–CO₃²⁻, 2–SO₄²⁻, 3–HSO₄⁻, 4–Br⁻, 5–I⁻, 6–NO₃⁻, 7–CH₃COO⁻, 8–SO₃²⁻, 9–H₂PO₄⁻, 10–HPO₄²⁻, 11–PO₄³⁻, 12–AMP, 13–ADP, 14–ATP). (d) The confocal fluorescence images of living HeLa cells and fixed HeLa cells with CZtpyZn. Scale bar: 20 μm. Reproduced from [70] with permission from Springer Nature, Copyright 2016.

b Detection of hydrogen peroxide (H₂O₂)

Common reactive oxygen species (ROS) are hydrogen peroxide (H₂O₂), superoxide anion (O²⁻) and singlet oxygen (¹O₂), which are endogenous metabolites that are indicators of oxidative stress. Among them, H₂O₂ can play an important role in physiological processes as a second messenger in intracellular signal transduction. However, H₂O₂ may be abnormally generated intracellularly when cells are stimulated by exogenous chemicals. The excessive H₂O₂ accumulates inside the cell, which will lead to oxidative damage to intracellular proteins, nucleic acids and liposomes. In the case of cancer, the DNA enriched in the nucleus is the most important target [71]. Once the oxidative damage of DNA is generated, such as cannot be repaired in a timely manner, it will induce the generation of gene mutations and eventually lead the cell to carcinogenesis or death [72]. Therefore, it is necessary to achieve sensitive detection of H₂O₂ in the nucleus. Chang's team discovered the nucleus-targeted H₂O₂ probe NucPE1 [73]. Interestingly, despite the absence of a specific targeting moiety, this probe can accumulate in the nucleus of several mammalian cell lines and *C. elegans*. Furthermore, once NucPE1 reacted with H₂O₂ in the cytoplasm, it lost its targeting ability, which enabled nucleus selective H₂O₂ imaging. Although the targeting mechanism remains to be further elucidated, this probe may serve as a novel fluorescent tool for monitoring the H₂O₂ flux in the nucleus. Moreover, Yi's team developed a versatile small molecule fluorescent probe NP1 that can be used for ratiometric detection of H₂O₂ (Figure 22a) [74]. NP1 mainly accumulated in the cytoplasm without adding to the nucleus. So, the transcription factor NF-κB derived sequence (VQRKRQKLMP-NH₂, named pep-1) was chosen as a NLS peptide for nuclear targeting modification of NP1. As shown in Figure 22b,c, pep-NP1 showed a ratiometric fluorescence response and good selectivity. More importantly, pep-NP1 achieved excellent nucleus targeting (Figure 22d) and enabled the detection of H₂O₂ levels inside the nucleus. However, how such probes avoid reacting with H₂O₂ inside the cytoplasm before entering the nucleus, is a matter for thought.

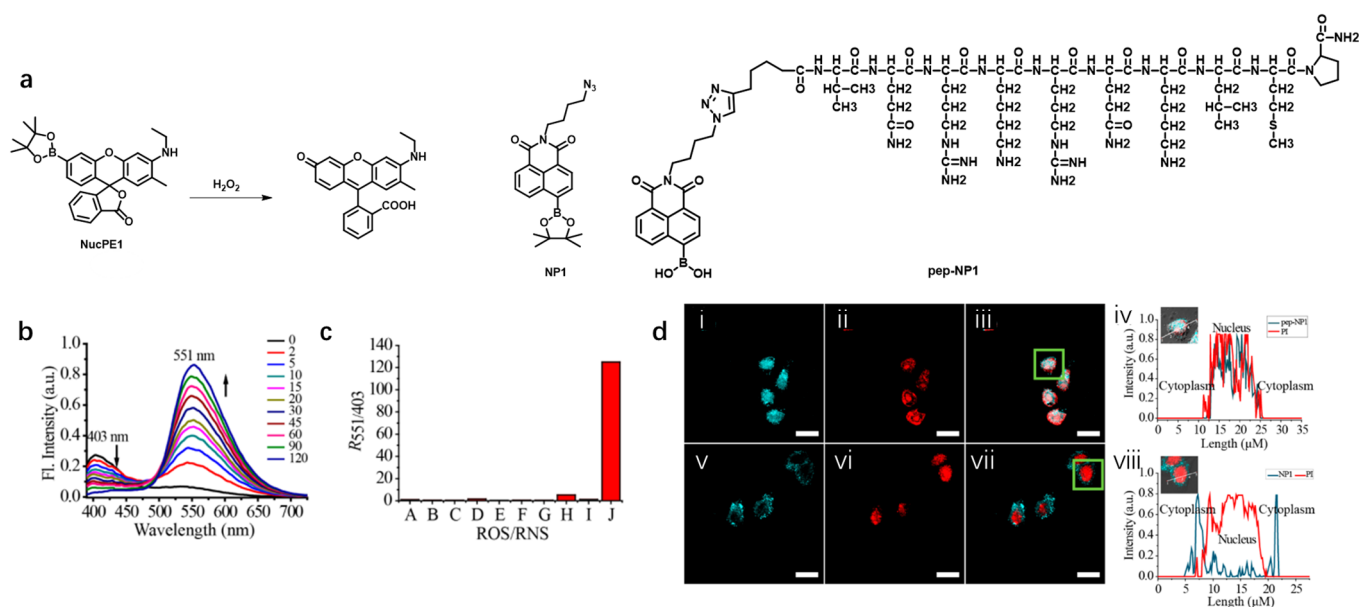


Figure 22. (a). The structures of NucPE1, NP-1 and pep-NP1. (b). Fluorescence spectral changes of pep-NP1 (5 μM) with time after addition of H_2O_2 (200 μM). (c). The fold change ($R_{551}/403$) of pep-NP1 (5 μM) to various ROS/RNS (200 μM) at 120 min. A to J represent none, tBHP, OCI^- , NO, $^1\text{O}_2$, HO \cdot , $\cdot\text{OtBu}$, $\text{O}_2^{\cdot-}$, $\text{O}^{2\cdot-}$ and H_2O_2 , respectively. (d). CLSM images of HeLa cells co-labeled (i–iii) with pep-NP1 (50 μM)/PI (1 nM) and (v–vii) with NP1 (5 μM)/PI (1 nM) at 37 $^\circ\text{C}$; (i,v) blue channel, (ii, vi) red channel and (iii,vii) the overlay images of blue and red channels; (iv,viii) cross-sectional analysis along the white line in the insets (amplified images of a single cell in green squares in (iii) and (vii), respectively). Blue channel: 445 ± 20 nm for NP1/pep-NP1; red channel: 625 ± 25 nm for PI. $\lambda_{\text{ex}} = 405$ nm; scale bar = 20 μm . Reproduced from [74] with permission from the American Chemical Society, Copyright 2014.

c Detection of Calcium Ions (Ca^{2+})

Calcium ions (Ca^{2+}) are very important for signal transduction in the cell interior, which through temporal and spatial fluctuations in concentration enable regulatory effects on a variety of biological processes [75]. Changes in the concentration of calcium ions in the nucleus can affect important life processes, such as gene expression, transport of nucleoprotein and RNA, degradation of DNA and nucleoprotein and cell division. Therefore, detecting the intranuclear Ca^{2+} content and change is of great significance for biological and medical research. Although many fluorescent indicators for Ca^{2+} have been reported so far, probes capable of detecting Ca^{2+} inside the nucleus are scarce. Zhu and coworkers developed a new red emitting and ratiometric Ca^{2+} fluorescent probe STDBT to measure Ca^{2+} at the nucleus and the cytosol [76]. STDBT is composed of 1,2-bis (2-aminophenoxy) ethane- N,N,N',N' -tetraacetic acid (BAPTA) units with a high Ca^{2+} selectivity and benzothiazolium hemicyanine dye with excellent spectral properties to construct an intramolecular charge transfer (ICT) structure (Figure 23) [77,78]. When Ca^{2+} is coordinated to BAPTA, it will induce conformational changes in the ICT structure and reduce the electron donating ability of aniline, leading to a blue shift in the spectra and an increase in the fluorescence intensity of STDBT. They further synthesized STDBT-AM (the tetra (acetoxymethyl) ester of STDBT) to increase the cellular permeability of the probe. STDBT-AM will be hydrolyzed by esterases contained in the cytoplasm after penetrating the cell membrane, thus reverting back to STDBT, which can detect Ca^{2+} . When Ca^{2+} was added to the STDBT buffer solution, an obvious ratiometric type response could be observed from the absorption and emission spectra of STDBT. Imaging results showed that STDBT was distributed in both the nucleus and the cytosol, delineating a very clear boundary between these two compartments. Thus, the probe can simultaneously distinguish Ca^{2+} changes

in the cytosol and nucleus of living cells. However, the mechanism of Ca^{2+} entering the nucleus remains unclear, more probes are needed to help reveal this. The characteristic properties of these probes in this section are summarized in Table 2.

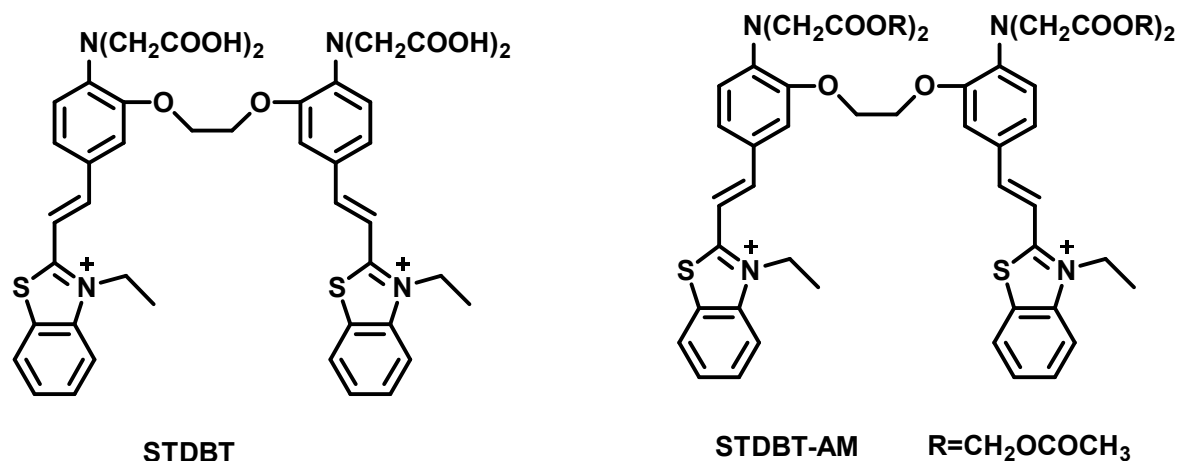


Figure 23. The chemical structures of STDBT and STDBT-AM.

Table 2. Summary of the characteristic properties of nucleus-targeted fluorescent probes for intranuclear biomolecule detection.

| Name [Ref.] | λ_{ex} (nm) | λ_{em} (nm) | Stokes Shift (nm) | Binding Constant | Fluorescent Quantum Yield | Species of Detection | Extinction Coefficient |
|----------------------|----------------------------|---|-------------------|--|---------------------------|----------------------|---|
| probe 8 [45] | 451 | 548 | 97 | $K_b = 2 \times 10^6 \text{ M}^{-1}$ (DNA d[A] ₁₀ :d[T] ₁₀) | 0.13 | DNA | — |
| probe 9 [46] | 430 | 585 | 155 | — | 0.024 | AT-rich DNA | $26,700 \text{ M}^{-1} \text{ cm}^{-1}$ |
| probe 10 [47] | 475 | 636 | 161 | — | 0.090 | DNA | $28,500 \text{ M}^{-1} \text{ cm}^{-1}$ |
| probe 11 [47] | 491 | 656 | 165 | — | 0.11 | DNA | $37,400 \text{ M}^{-1} \text{ cm}^{-1}$ |
| probe 12 [47] | 491 | 665 | 174 | — | 0.12 | DNA | $66,000 \text{ M}^{-1} \text{ cm}^{-1}$ |
| PA1 (probe 13) [48] | 473 | 522 | 49 | $7.3 \times 10^2 \text{ M}^{-1}$ | 0.008 | DNA | $41,200 \text{ M}^{-1} \text{ cm}^{-1}$ |
| PA2 (probe 13) | 480 | 560 | 80 | $5.9 \times 10^2 \text{ M}^{-1}$ | 0.009 | DNA | $38,700 \text{ M}^{-1} \text{ cm}^{-1}$ |
| PA3 (probe 13) | 454 | 490 | 36 | $1.2 \times 10^3 \text{ M}^{-1}$ | 0.010 | DNA | $38,600 \text{ M}^{-1} \text{ cm}^{-1}$ |
| PA4 (probe 13) | 481 | 520 | 39 | $2.4 \times 10^3 \text{ M}^{-1}$ | 0.030 | DNA | $49,200 \text{ M}^{-1} \text{ cm}^{-1}$ |
| PA5 (probe 13) | 504 | 534 | 30 | $7.4 \times 10^3 \text{ M}^{-1}$ | 0.070 | DNA | $29,600 \text{ M}^{-1} \text{ cm}^{-1}$ |
| probe 14 [49] | 340 | 406; 490 | 66; 150 | $2 \times 10^5 \text{ M}^{-1}$ (p(dA·dT) ₂) $3 \times 10^4 \text{ M}^{-1}$ (p(dG·dC) ₂) | — | AT-rich DNA | — |
| QPP-AS [50] | 405; 488 (in DCM) | 500 and 650; 650 (in DCM) | — | — | — | DNA | $22,900 \text{ M}^{-1} \text{ cm}^{-1}$; $54,300 \text{ M}^{-1} \text{ cm}^{-1}$ (in DCM) |
| NBE [52] | 618 | 680 | 62 | — | 0.040 | RNA | — |
| BIQ [53] | 611 | 657 | 46 | $1.2 \times 10^8 \text{ M}^{-1}$ | 0.010 | RNA | — |
| probe 15 [54] | 444 | 545 | 101 | — | 0.0378 | rRNA | $11,250 \text{ M}^{-1} \cdot \text{cm}^{-1}$ |
| INR1 (probe 16) [56] | 467 | 533 (single-fluorescent peak); 540 (two-photo fluorescent peak) | 66; 73 | — | 0.028 | RNA | $25,000 \text{ M}^{-1} \text{ cm}^{-1}$ |

Table 2. Cont.

| Name [Ref.] | λ_{ex} (nm) | λ_{em} (nm) | Stokes Shift (nm) | Binding Constant | Fluorescent Quantum Yield | Species of Detection | Extinction Coefficient |
|----------------------|----------------------------|--|-------------------|---|---------------------------|-------------------------------|--|
| INR2 (probe 16) [56] | 465 | 532 (single-fluorescent peak); 540 (two-photo fluorescent peak) | 67; 75 | — | 0.027 | RNA | 25,000 M ⁻¹ cm ⁻¹ |
| MR-IDE [55] | 438 (in DMF) | ~531 (in DMF) | ~93 | — | 0.0157 | mtRNA | — |
| TAB [57] | 405 | 560 | 155 | — | 0.500 (in DMSO) | RNA | — |
| 4a [58] | 475 | 630 | 155 | $9.65 \times 10^5 \text{ M}^{-1}$ | 0.170 | GQ | — |
| SQgI [59] | 660 | 744 | 84 | $\sim 10^5 \text{ M}^{-1}$ | 0.610 | Parallel GQ | — |
| CAS-C1 [60] | 698 | 720 | 22 | $9.7 \times 10^6 \text{ M}^{-1}$ | ~0.700 | Parallel GQ | ~90,000 M ⁻¹ cm ⁻¹ |
| K21 [65] | 426 | 480 | 54 | $6.32 \times 10^6 \text{ M}^{-1}$ (10AT dsDNA) | — | AT-rich DNA | — |
| Rh-Gly [66] | 365 | 585 | 220 | — | — | H2B | — |
| BOXTO-GK(Ac)G [68] | 520 | 545 | 25 | $\sim 1.41 \times 10^6 \text{ M}^{-1}$ | — | HADCs | — |
| probe 17 [69] | 499 | 523 | 24 | — | — | HADCs | — |
| CZtpyZn [70] | 400 | 515 | 115 | — | — | PPi | — |
| NucPE1 [73] | 505 | 530 | 25 | — | 0.626 | H ₂ O ₂ | 19,100 M ⁻¹ cm ⁻¹ |
| NP1 [74] | 446 | 555 | 109 | — | 0.087 | H ₂ O ₂ | 10,820 M ⁻¹ cm ⁻¹ |
| pep-NP1 [74] | 403 | 551 | 148 | — | — | H ₂ O ₂ | ~5900 M ⁻¹ cm ⁻¹ |
| STDBT [76] | 506 | 600 | 94 | $1.32 \times 10^3 \text{ M}^{-1}$ | — | Ca ²⁺ | — |

4.3. Application of Nucleus-Targeted Fluorescent Probes in Theranostics

Photodynamic therapy (PDT) is currently emerging in the clinic as a novel treatment. PDT generated reactive oxygen species (ROS) have a very short half-life (20 ns), which renders their radius of action very short (20 nm). The cytoplasm is rich in a large amount of reducing substances, such as GSH, which is able to quench singlet oxygen, thus leading to poor PDT treatment efficacy. However, ROS can easily damage nucleic acids within the nucleus, leading to cell death. Therefore, developing photosensitizers with nucleus targeting ability will greatly improve the PDT therapeutic effect. Several nucleus-targeted organic photosensitizers are mainly introduced below for tumor therapy. The characteristic properties of these probes in this section are summarized in Table 3.

In 2021, Liu and coworkers developed a nucleus-targeted AIE photosensitizer, MeTPAE, which achieved nucleus-targeted PDT treatment by interacting with DNA and histone deacetylases (HDACs) inside the nucleus [79]. The structure of MeTPAE is shown in Figure 24, with the positively charged cationic pyridine unit on the left facilitating electrostatic binding between MeTPAE and nucleic acids, and its 'Y'-shaped structure facilitating intercalation into DNA; The hydroxamic acid chelating group on the right serves to chelate the zinc ion at the active center of HDACs. In addition, Zhang et al. developed a nucleus-targeted organic iridium human serum albumin (Ir1-HSA) conjugate for PDT cancer therapy [80]. Studies have shown that albumin appears to play an important role in the transport and delivery of Ir1 to the nucleus. Ir1-HSA has a very high quantum yield of ¹O₂ generation as well as high photostability, and exhibits good photocytotoxicity against a range of cancer cell strains and multicellular spheroids.

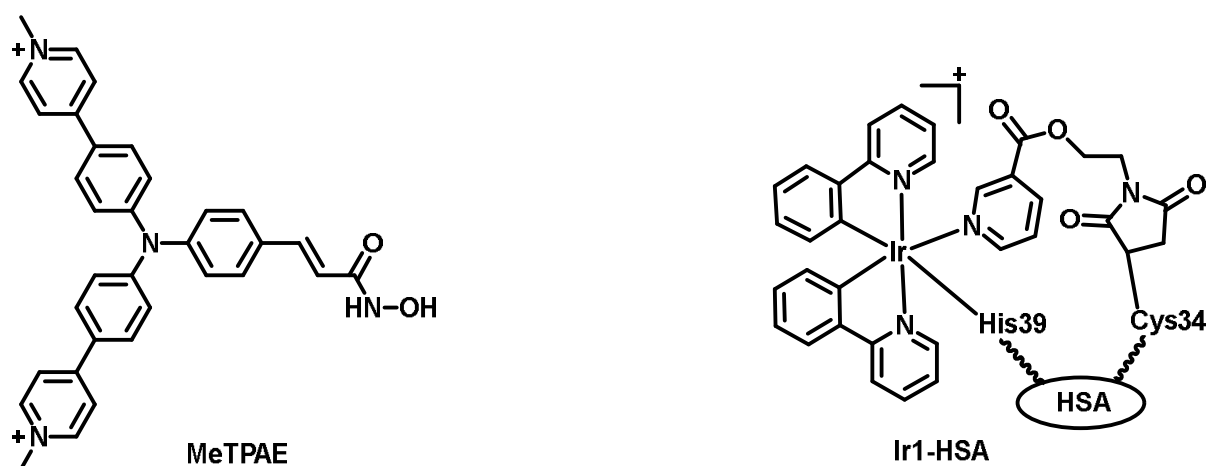


Figure 24. Structures of MeTPAE and Ir1-HSA.

PDT exhibits selective cytotoxicity to cancer cells with high spatiotemporal precision and noninvasiveness. However, PDT also shows some disadvantages. For example, highly active photosensitizers and high-power light can destroy normal cells, affecting the efficacy of treatment [81]. Therefore, it is important to achieve synchronous monitoring of the anticancer efficacy of PDT to prevent overtreatment. Gao et al. developed a bifunctional photosensitizer TPCI [82], which could not only effectively ablate cancer cells, but also report anticancer effects in real time from the beginning of the treatment (Figure 25a). TPCI exhibits weak fluorescence in the nuclei before light irradiation, induces cell death due to singlet oxygen generation after light irradiation, and then immediately emits a strong fluorescence signal in the nuclei of dead cells, as a way to achieve accurate and efficient real-time reporting of the cell death situation (Figure 25b). Different from TPCI, Zhang et al., to avoid therapeutic overdosing by monitoring the process of PDT, induced apoptosis and developed a self-report photosensitizer, TPE-4EP+ (Figure 25c), for monitoring the apoptotic process in situ [83]. TPE-4EP+ translocated from mitochondria to the nucleus during PDT induced apoptosis, which was monitored in real time in situ by observing fluorescence migration (Figure 25d). In short, these photosensitizers have short excitation and emission wavelengths and insufficient penetration ability into biological tissues. In addition, its biosafety remains to be examined.

Improved Strategies for Nucleus-Targeted Delivery Efficiency of Drugs or Probes

The nucleus, as a control center for cellular genetic information and metabolism, is an optimal anticancer drug target. Many chemotherapeutic drugs used clinically, such as doxorubicin (DOX), cisplatin and hydroxycamptothecin (HCPT), mainly function in the nucleus. Unfortunately, the nucleation capacity of these drugs is poor. Moreover, the reactive oxygen species (ROS) generated by the photosensitizer activated by light, which is easily quenched in aqueous solution with limited diffusion distance, have a stronger killing effect in the nucleus. Therefore, nuclear targeting can effectively improve the anticancer effects of therapeutic drugs that function in the nucleus. However, various physiological barriers are faced for drugs to enter the nucleus, which makes drug delivery very inefficient to achieve good therapeutic effects. To address this, several strategies have been proposed to improve nuclear drug delivery, such as chemical modification of drugs, covalent conjugation to units that target or penetrate cells and nanoparticle formulations. Currently developed methods are bioconjugation techniques, endogenous vesicle (i.e., exosome) loading, nanoparticle carriers, etc.

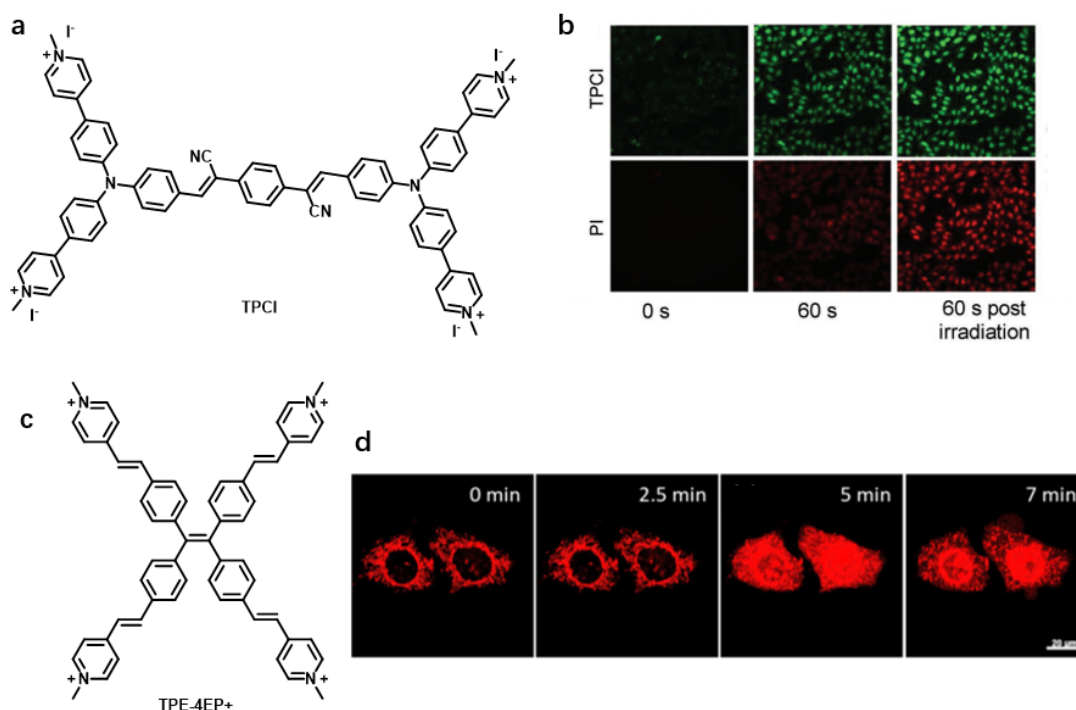


Figure 25. (a) The structure of TPCI. (b) Fluorescence microscopic images of TPCI-pretreated HeLa cells co-stained with propidium iodide (PI) at different irradiation times and post irradiation. (460 nm, 18 mW/cm²), TPCI channel: ($\lambda_{\text{ex}} = 460\text{--}490$ nm), PI channel: ($\lambda_{\text{ex}} = 510\text{--}550$ nm). (c) The structure of TPE-4EP+. (d) Real-time confocal imaging of HeLa Cells under continuous 405 laser irradiation stained with TPE-4EP+. Reproduced from [82,83] with permission from John Wiley and Sons, Copyright 2019 and the American Chemical Society, Copyright 2019 respectively.

Bioconjugation is simply the attachment of one molecule to another often by covalent bonds to produce a complex in which two molecules are held together. Bioconjugation is a promising research area due to its wide application in the development of novel technologies concerning specific target derivatized proteins, DNA, RNA and carbohydrates, such as ligand discovery, disease diagnosis and efficient screening. Lipids, aptamers, cell targeting and cell penetrating peptides and sugars have been developed to improve nuclear delivery efficiency.

Oligonucleotide therapy, one of the approaches for cancer treatment, which can prevent many erroneous gene expressions by precisely repressing some genes, or silencing the genes with aberrant coding, has received increasing attention in cancer and other diseases. Currently, the known oligonucleotide drugs mainly include antisense oligonucleotides (ASO), small interfering ribonucleic acid (siRNA), microRNAs (miRNA), nucleic acid aptamers (aptamers) and so on. However, a major hurdle currently facing oligonucleotide therapeutics is the difficulty in efficiently delivering drugs to target organs and tissues. Xia and coworkers synthesized T_DNCP that can be used for real-time tracking, efficient and sequential targeted delivery of ASO into the nucleus by conjugating multiple functional peptides on the aggregation induced luminophores (AIEgen) [84]. T_DNCP mainly include four parts (Figure 26): (1) Cancer cell targeting peptide (DGR), which is an integrin $\alpha_v\beta_3$ targeting ligand for the receptor. Integrin receptors are highly expressed on a variety of tumor cells, such as breast and cervical cancer cells. (2) Nuclear localization signal (KRRRR), which plays an important role in nucleocytoplasmic transport through the nuclear pore complex. (3) Cell penetrating peptide (RRRR), which mainly consists of 4 to 9 positively charged amino acids, is used to deliver cell impermeable cargo into the cell or nucleus and improve endosomal escape ability. (4) One AIE based molecule (PyTPE), is an azide functionalized tetraphenylethylene derivative with good fluorescence properties for cellular imaging. Moreover, PyTPE can enhance the hydrophobicity of T_DNCP to stimulate self-assembly

ability. Based on the above four parts, T_DNCP can efficiently encapsulate therapeutic genes, achieving sequential targeted delivery in the nucleus and real-time tracking.

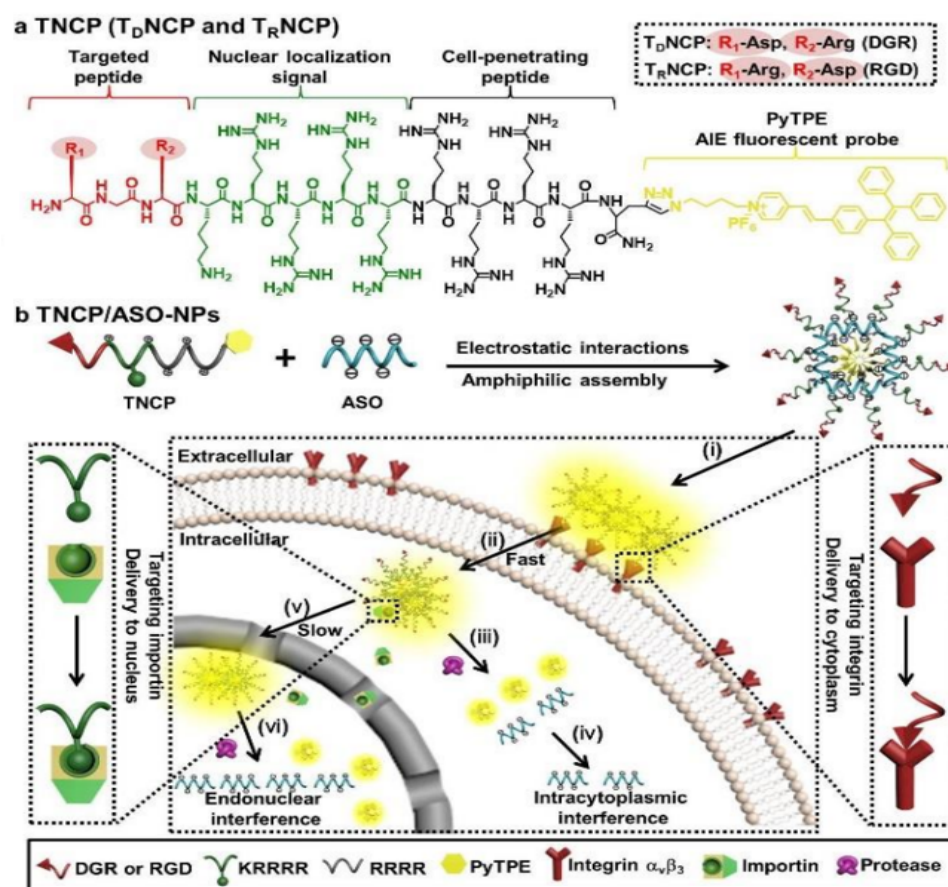


Figure 26. Illustration of TNCP and TNCP/ASO self-assembled nanoparticles (TNCP/ASO-NPs). (a) Molecular structure of TNCP including T_DNCP and T_RNCP. (b) TNCP/ASO-NPs are used for real-time tracking the efficient and sequential targeted delivery into the nucleus. (i) Selective bind to integrin $\alpha_v\beta_3$; (ii) rapid entry into the cytoplasm; (iii) partially degraded by protease and disassembly in the cytoplasm; (iv) partial ASO released into the cytoplasm and performed intracytoplasmic interference; (v) selective combination with importin and transported into the nucleus; (vi) most of ASO released in the nucleus and performed endonuclear interference. Reproduced from [84] with permission from John Wiley and Sons, Copyright 2019.

Ru (II) complexes containing polyazaaromatic ligands can be better characterized for their interaction with DNA and thus have long been investigated as DNA sensors or photodynamic therapy (PDT) agents. Keyes and coworkers have used nuclear factor-kappa B (NF- κ B, a transcription factor peptide) conjugated Ru (II)-bis-tap complex (tap = 1,4,5,8-tetraazaphenanthrene) and successfully achieved nucleus specific targeting of living HeLa and CHO cells [85]. Ru (II) complexes containing two tap ligands have sufficiently positive excited state reduction potentials to serve the purpose of DNA damage by photoinduced electron transfer for oxidation of guanine in DNA. Remarkably, this Ru-tap probe can achieve the precise killing of individual cells with excellent spatiotemporal control over the ability to induce cell destruction (Figure 27b). The aforementioned are all the modifications of NLS peptide to increase the nuclear targeting ability, in fact, the modification of glycosyl can also enhance the nuclear targeting ability of drugs or probes. In 2020, Scott's team developed a very effective method to conjugate sugar groups with triple complexed metal helices, and the synthesized products have amphiphilic structures and are very stable in both water and biological media [86]. In addition, studies found that combining glucose derivatives has the best selectivity and can better increase the nuclear targeting ability.

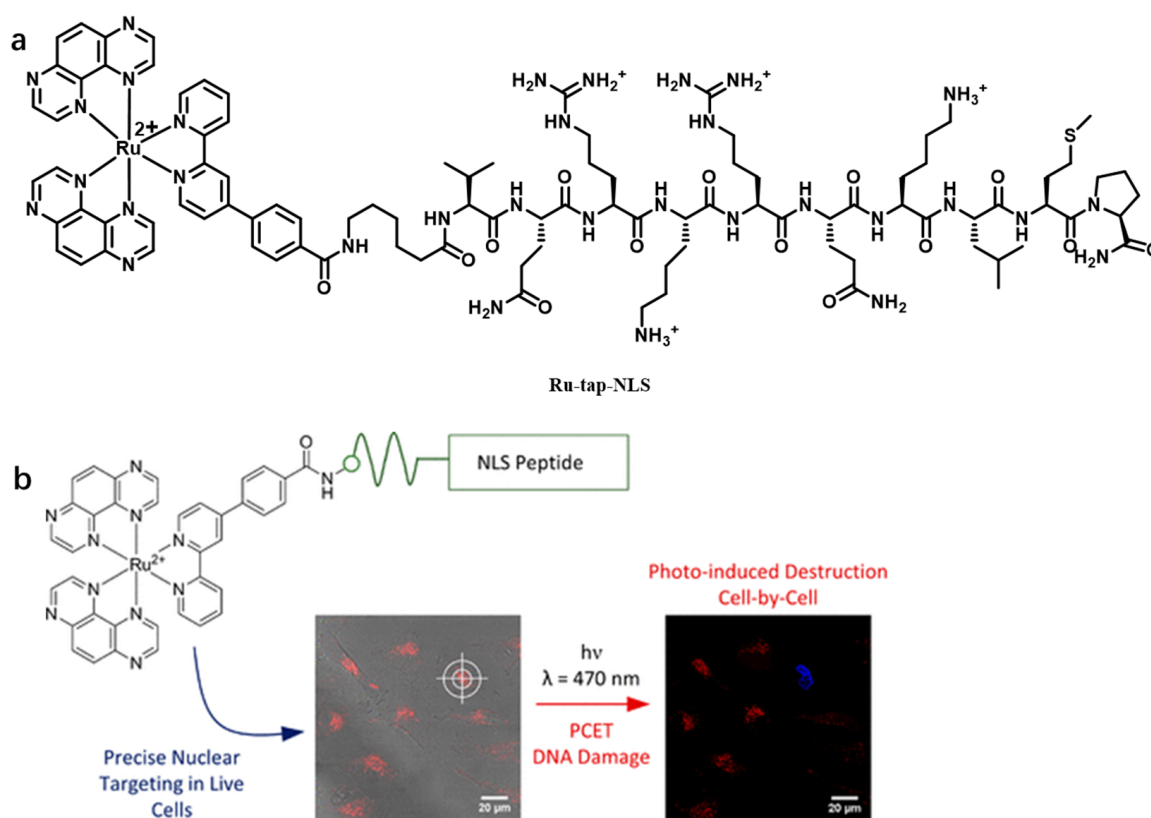


Figure 27. (a) Structures of Ru-tap-NLS. (b) Ru-tap-NLS probe can precisely kill single HeLa cells at 470 nm (0.13 mW/cm^2). Reproduced from [85] with permission from the American Chemical Society, Copyright 2018.

Exosomes, that are a kind of natural nanovesicles that can be endogenously secreted by mammalian cells, have been regarded as a very suitable platform for drug delivery due to their good biocompatibility and low immunogenicity. Li et al. developed a multifunctional chimeric peptide engineered exosome (ChiP-EXO) for dual stage light induced plasma membrane and nucleus-targeted photodynamic therapy [87]. Among them, multifunctional chimeric peptides engineered exosome consist of three parts: (1) alkyl chains: for exosome engineering; (2) PpIX photosensitizer; (3) nuclear localization signal (NLS) peptide (Figure 28a). As shown in the Figure 28b, ChiP-EXO is partially targeted to the cell membrane and a portion enters the cell interior via endocytosis. When the first stage light irradiation was performed, ChiP-EXO fused on the membrane and generated reactive oxygen species in situ on the membrane to destroy the cell membrane structure and thus cause cell death; In parallel, ChiP-EXO were released from lysosomes and targeted to the nucleus. Due to the disruption of the cell membrane structure, so that ChiP-EXO can also directly enter the cytoplasm by diffusion and then target to the nucleus. CLSM image results confirms the translocation process of ChiP-EXO from the cytoplasm to the nucleus after the first stage of light irradiation. Subsequently, a second stage of light irradiation PDT treatment was performed, ChiP-EXO entering the nucleus was excited to generate ROS in situ to destroy the nucleus. The tumor targeting efficiency was made high by the dual-stage photoirradiation strategy, which well improved the PDT treatment efficiency. This synergistic PDT dual targeting strategy based on exosomes may open a window for the development of biologically derived nanomedicines for precision tumor therapy.

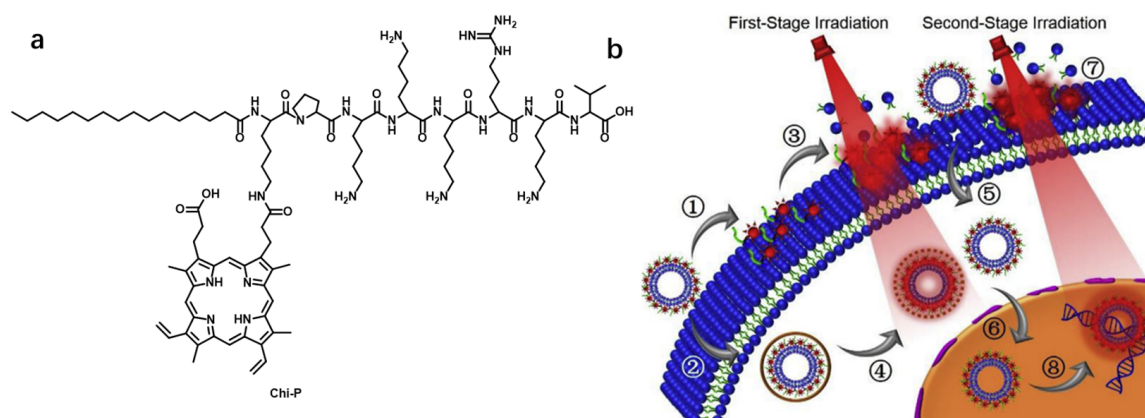


Figure 28. (a) Chemical structure of ChiP. (b) The proposed processes of ChiP-Exo for dual-stage light guided plasma membrane and nucleus-targeted PDT. ① Plasma membrane targeted delivery of ChiP-Exo; ② The intracellular delivery of ChiP-Exo through endocytosis; ③ Plasma membrane fluctuation and ④ lysosomal escape of ChiP-Exo under the first-stage light irradiation; ⑤ Photochemical internalization (PCI) of ChiP-Exo; ⑥ Nucleus targeted translocation of ChiP-Exo; ⑦ Plasma membrane rupture and ⑧ nucleus destruction under the second-stage light irradiation.

To solve the problem of inefficient nuclear delivery of drugs, various nanoparticle carriers were developed. In 2012, Pan et al. were the first to couple TAT peptide onto mesoporous silica nanoparticles with high efficient drug loading capacity for nucleus-targeted drug delivery [88]. In the same year, Xu and coworkers designed a poly(2-(pyridin-2-yl)disulfanyl) ethyl acetate (PDS) based nanoparticle delivery system [89]. Polyethylene glycol and cyclic (ArG-Gly-Asp-D-Phe-Cys) (cRGD) peptide were combined with PDS via thiol disulfide exchange reaction to obtain RPDSG polymer, a pH- and redox dual responsive nanoparticle that can be used for nucleus-targeted drug delivery. In 2018, a novel DNA nanostructure based on the coordination between calcium ions (Ca^{2+}) and AS1411 DNA G-quadruplex to form nanocoordinating polymers (NCPs) was developed by Yu Yang et al. [90]. Figure 29a shows the Ca-AS1411/Ce6/hemin@pHis-PEG preparation and nuclear targeting process of (CACH-PEG) NCP nanostructures. Among them, chlorine e6 (Ce6) is a photosensitizer; hemin is an iron containing porphyrin; The AS1411 aptamer is single stranded DNA with specific recognition ability for nucleolin (a non-ribosomal protein in the nucleus) that can bind hemin to form a G-quadruplex-galactose DNAzyme and display high catalase-like activity, and this enzyme can trigger the decomposition of endogenous H_2O_2 to generate O_2 appropriately to relieve tumor hypoxia, thus further overcoming hypoxia related PDT resistance. In addition, AS1411 also inhibited the expression of anti-apoptotic protein B-cell lymphoid carcinoma 2 (Bcl-2). When the NCPs enter the cells through endocytosis, the acidic environment of lysosomes will break down the NCPs, thus achieving the inhibition of the intranuclear transport of Ce6 and the expression of anti-apoptotic Bcl-2. This nanosystem can achieve intranuclear delivery of photosensitizers, downregulation of anti-apoptotic proteins, and simultaneous modulation of unfavorable tumor microenvironment for improved cancer therapy. In 2019, Chen and coworkers developed a novel universal platform for direct nuclear delivery based on C_5N_2 nanoparticles (Figure 29b) [91]. The supramolecular interaction between C_5N_2 NPs and the cell membrane can enhance the cellular uptake; The abundant marginal amino groups prompted the rapid and efficient fragmentation of early endosomes to release the drug and readily targeted them to the nucleus. The results demonstrate that this platform can, not only deliver molecular drugs (doxorubicin, HCPT, and propidium iodide) and MnO_2 nanoparticles efficiently to the nucleus, but also be light responsive for nucleus-targeted photothermal therapy (PTT) and photodynamic therapy (PDT), thus further improving the anticancer efficacy.

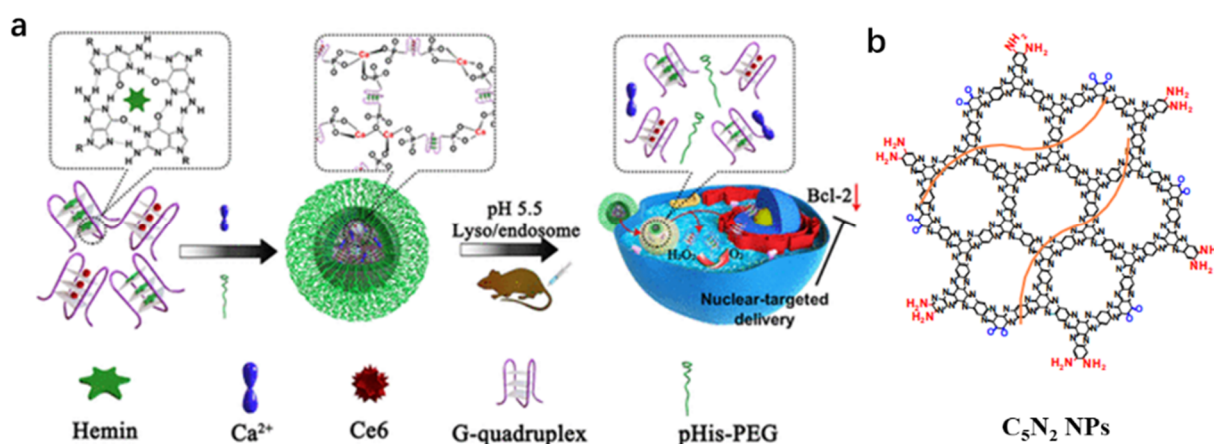


Figure 29. (a). Schematic illustration for the synthesis of CACH-PEG. (b) Structure of C₅N₂ NPs. Reproduced from [90,91] with permission from the ACS, Copyright 2018 and John Wiley and Sons, Copyright 2019, respectively.

In 2019, a new graphene based tumor cell nucleus-targeted fluorescent nanoprobe (GTTN) was developed by Wang et al., and a novel cell membrane permeable targeting (CMPT) mechanism was proposed [92]. Notably, this probe not only possesses excellent tumor targeting ability (approximately 50% tumor targeting rate), but also specifically targets tumor cell nuclei. GTTN identifies tumor cells and normal cells by differences in cell membrane permeability between normal and tumor cells. GTTN can penetrate tumor cell membranes without crossing normal cell membranes. Once GTTN enters tumor cells, it binds to DNA and histones and finally targets tumor cell nuclei. The spatial structure of GTTN is shown in Figure 30a. GTTN was functionalized with sulfonic acid groups and hydroxyl groups with some Na⁺ existing between the interlayer to maintain this spacing, preventing graphene from expanding when immersed in aqueous solution. Confocal imaging results showed that GTTN possessed good nuclear targeting function in tumor tissues (Figure 30b), while in normal tissues, GTTN only stayed in the intercellular space and could not cross the cell membrane (Figure 30c). This study shows for the first time that nanomaterials can directly recognize tumor cells by specifically targeting the nucleus without traversing the normal cell membrane. This highly efficient and accurate tumor cell targeting technology will accelerate the arrival of a new era of tumor diagnosis and treatment.

Table 3. Summary of characteristic properties of nucleus-targeted fluorescent probes for therapy.

| Name [Ref.] | λ_{ex} (nm) | λ_{em} (nm) | Stokes Shift (nm) | Binding Constant | Fluorescent Quantum Yield | ¹ O ₂ Quantum Yield | Lifetime | Extinction Coefficient |
|-----------------|----------------------------|----------------------------|-------------------|--|---------------------------|---|----------|---|
| MeTPAE [79] | 424 | 632 | 208 | $\sim 4.52 \times 10^5 \text{ M}^{-1}$ (dsDNA); $\sim 1.70 \times 10^6 \text{ M}^{-1}$ (G4) | — | 0.772 | — | $39,400 \text{ M}^{-1} \text{ cm}^{-1}$ |
| Ir1-HAS [80] | 405 | 515 | 110 | — | 0.036 | 0.830 | 871.8 ns | — |
| TPCI [82] | 441 | ~ 580 | 139 | $5.68 \times 10^8 \text{ M}^{-1}$ | 0.03 | 0.986 | — | — |
| TPE-4EP+ [83] | 405 | 610 | 205 | — | 0.15 | — | — | — |
| Ru-tap-NLS [85] | 415 | 640 | 225 | $2.26 \times 10^7 \text{ M}^{-1}$ | 0.028 | — | 760 ns | $16,700 \text{ M}^{-1} \text{ cm}^{-1}$ |
| GTTN [92] | ~ 500 | ~ 520 | ~ 20 | — | 0.4179 | — | — | — |

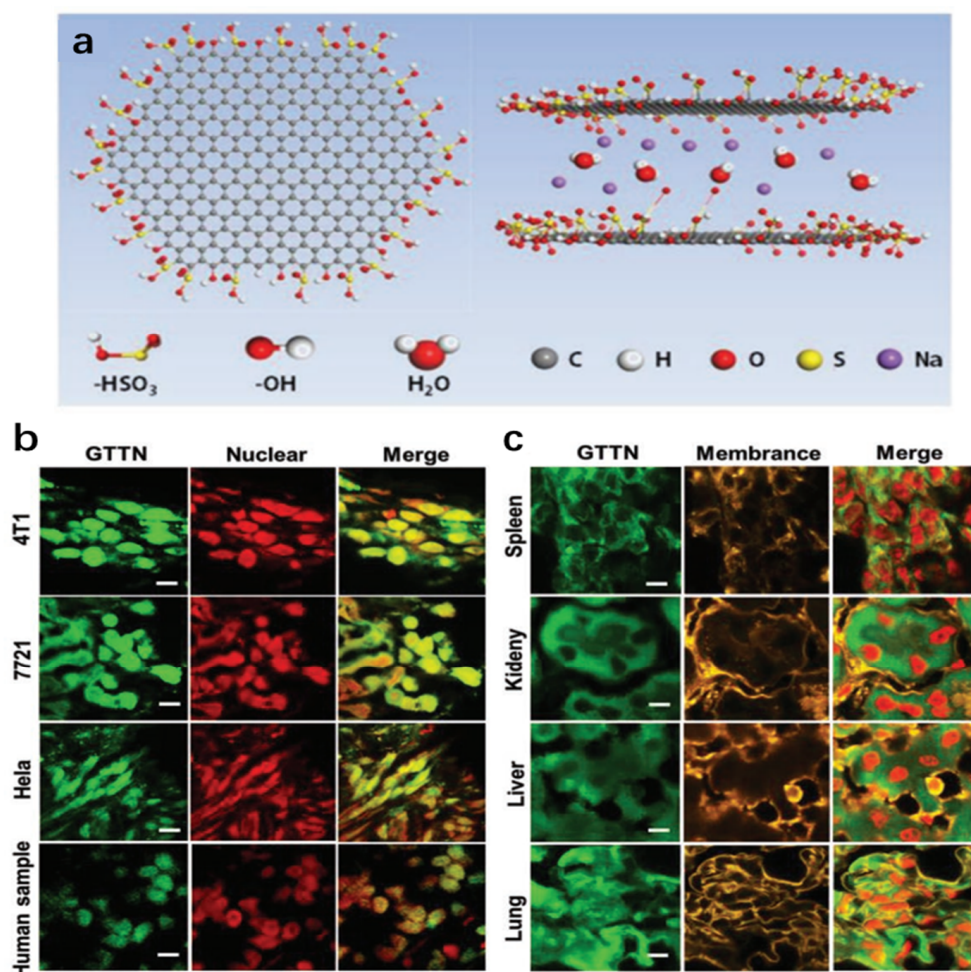


Figure 30. (a) The spatial structure of GTTN. (b) Tumor tissue frozen section of subcutaneous tumor model and human hepatoma tumor model. (c) Normal tissue frozen section of subcutaneous tumor model. Reproduced from [92] with permission from John Wiley and Sons, Copyright 2019.

5. Conclusions and Perspectives

In the past decades, considerable progress has been made in the development of a small-molecule nucleus-targeted fluorescent probe. These probes provide a powerful means to better understand the roles of the nucleus in the physiological and pathological processes of cells, as well as the study of intranuclear biomolecule functions during cancer diagnosis and treatment. In this review, we summarized recent advances in this promising field, including the current general strategies for designing nucleus-targeted fluorescent probes, and the applications of nucleus-targeted fluorescent probes in nuclear imaging, intranuclear biomolecular detection (e.g., DNA, RNA, Ca^{2+} , H_2O_2 , etc.) and cancer therapy. Although many well-performing nucleus-targeting fluorescent probes have been developed in recent years for use in biological and medical research, the field still faces several challenges: Firstly, there are few general strategies for designing nucleus-targeted fluorescent probes and the specificity of these probes is usually unsatisfactory. Design strategies for cation-based fluorescent dyes of the nucleus tend to have mitochondrial targeting capabilities because this class of positively charged lipid soluble probes is also readily enriched in mitochondria. In addition, the basic NLS peptide may be trapped in lysosomes and readily hydrolyzed or inactivated by multiple proteases *in vivo*. Therefore, it is essential to develop novel methodologies for constructing novel nucleus-targeted probes with high specificity. Secondly, the mechanism of many nucleus-targeted fluorescent probes without using NLS entering the nucleus is still unclear, which is one of the unsolved difficulties in the field. Subtle changes in the structure of the probe may lead to a significant reduction in targeting

efficacy. The number of hydrophilic cations contained in the molecular structure, the length of the hydrophobic chain, and the size of the planar aromatic system can all affect the nuclear targeting effect of the probe. Therefore, in-depth study of the mechanism of these probes into the nucleus will be very critical for the development of nucleus targeted fluorescent probes. Thirdly, for the imaging of nucleus, it is essential to note the brightness, lifetime, penetration depth, high spatiotemporal resolution and ability to avoid autofluorescence from the surrounding environment. Therefore, it is imperative to appreciate the promising potential of two-photon and NIR probes for nuclear imaging. Moreover, although some fluorescent probes have been developed which can be used for the detection of biomolecules (such as DNA, RNA, G-quadruplex, H2B, Ca²⁺, H₂O₂, etc.) in the nucleus, the number is small, and in a part of the probes, there still exist problems with the unclear detection mechanism. In addition, there are many other kinds of biomolecules (such as various biological enzymes and proteins) in the nucleus, and they have not yet been developed with suitable fluorescent probes to detect them. Consequently, there is still much room for the development of fluorescent probes for the detection of biomolecules inside the nucleus. In terms of medical applications, whether the effect of nucleus-targeted therapy is higher compared with other treatments requires more favorable evidence. Although many kinds of nucleus-targeted drugs have been developed so far, their nuclear delivery efficiency is unsatisfactory (whether based on active targeting or passive targeting strategies). Therefore, it is still necessary to develop novel nucleus-targeted mechanisms to further improve the delivery efficiency of nucleus-targeted drugs. Moreover, probes with the functions of multiparametric detection and multimodal imaging are still scarce. Last but not the least, nucleic acid bounding fluorescent probes, such as DAPI and Hoeschest, may affect the normal function of the nucleus. Their cytotoxicity should be comprehensively studied and not simply be evaluated by testing the cell survival rate after 24 or 48 h treatment with these dyes. We believe relevant investigations will greatly accelerate diagnosis and treatment.

In summary, over the past few decades, a great deal of research has been devoted to the development of nucleus-targeted fluorescent probes, focusing on the preparation of robust fluorescent tools to improve the resolution and sensitivity during cellular imaging and to better explain the molecular mechanisms of various biological events. However, studies on nucleus-targeted fluorescent probes are currently immature, and many questions remain to be addressed. It is believed that with the joint efforts of a wide range of researchers, more efficient and higher performance nucleus-targeted fluorescent probes will be developed in the future for further understanding the pathogenesis of nuclei and their related diseases, to inject energy for the development of chemistry, biology, medicine and other fields.

Author Contributions: Methodology, C.H.; investigation, C.H.; writing—original draft preparation, C.H., H.L. (Haixia Li) and Z.S.; writing—review and editing, H.L. (Hongwen Liu) and S.X.; supervision, H.L. (Hongwen Liu); project administration, H.L. (Hongwen Liu); funding acquisition, H.L. (Hongwen Liu) and S.X. All authors have read and agreed to the published version of the manuscript.

Funding: This research was funded by the National Natural Science Foundation of China (Grants 22104036) and Shandong Key Laboratory of Biochemical Analysis (SKLBA2107).

Institutional Review Board Statement: Not applicable.

Informed Consent Statement: Not applicable.

Data Availability Statement: Not applicable.

Acknowledgments: We gratefully acknowledge the support of this work by the National Natural Science Foundation of China (Grants 22104036) and Shandong Key Laboratory of Biochemical Analysis (SKLBA2107).

Conflicts of Interest: The authors declare no conflict of interest.

References

1. Cheng, Y.; Sun, C.; Ou, X.; Liu, B.; Lou, X.; Xia, F. Dual-targeted peptide-conjugated multifunctional fluorescent probe with AIEgen for efficient nucleus-specific imaging and long-term tracing of cancer cells. *Chem. Sci.* **2017**, *8*, 4571–4578. [[CrossRef](#)]
2. Zhou, X.; Hao, Q.; Zhang, Q.; Liao, J.m.; Ke, J.w.; Liao, P.; Cao, B.; Lu, H. Ribosomal proteins L11 and L5 activate TAp73 by overcoming MDM2 inhibition. *Cell Death Differ.* **2015**, *22*, 755–766. [[CrossRef](#)] [[PubMed](#)]
3. Peleg, S.; Feller, C.; Ladurner, A.G.; Imhof, A. The metabolic impact on histone acetylation and transcription in ageing. *Trends Biochem. Sci.* **2016**, *41*, 700–711. [[CrossRef](#)] [[PubMed](#)]
4. Futscher, B.W.; Oshiro, M.M.; Wozniak, R.J.; Holtan, N.; Hanigan, C.L.; Duan, H.; Domann, F.E. Role for DNA methylation in the control of cell type-specific maspin expression. *Nat. Genet.* **2002**, *31*, 175–179. [[CrossRef](#)] [[PubMed](#)]
5. Olson, K.J.; Ahmadzadeh, H.; Arriaga, E.A. Within the cell: Analytical techniques for subcellular analysis. *Anal. Bioanal. Chem.* **2005**, *382*, 906–917. [[CrossRef](#)]
6. Lichtman, J.W.; Conchello, J.-A. Fluorescence microscopy. *Nat. Meth.* **2005**, *2*, 910–919. [[CrossRef](#)]
7. Cotruvo, J.J.A.; Aron, A.T.; Ramos-Torres, K.M.; Chang, C.J. Synthetic fluorescent probes for studying copper in biological systems. *Chem. Soc. Rev.* **2015**, *44*, 4400–4414. [[CrossRef](#)]
8. Alamudi, S.H.; Satapathy, R.; Kim, J.; Su, D.; Ren, H.; Das, R.; Hu, L.; Alvarado-Martínez, E.; Lee, J.Y.; Hoppmann, C.; et al. Development of background-free tame fluorescent probes for intracellular live cell imaging. *Nat. Commun.* **2016**, *7*, 11964. [[CrossRef](#)]
9. Horobin, R.W.; Stockert, J.C.; Rashid-Doubell, F. Fluorescent cationic probes for nuclei of living cells: Why are they selective? A quantitative structure–activity relations analysis. *Histochem. Cell Biol.* **2006**, *126*, 165–175. [[CrossRef](#)]
10. Chen, T.R. In situ detection of mycoplasma contamination in cell cultures by fluorescent Hoechst 33258 stain. *Exp. Cell Res.* **1977**, *104*, 255–262. [[CrossRef](#)]
11. Kapuscinski, J. Dapi: A DNA-specific fluorescent probe. *Biotech. Histochem.* **1995**, *70*, 220–233. [[CrossRef](#)]
12. Ishida, M.; Watanabe, H.; Takigawa, K.; Kurishita, Y.; Oki, C.; Nakamura, A.; Hamachi, I.; Tsukiji, S. Synthetic self-localizing ligands that control the spatial location of proteins in living cells. *J. Am. Chem. Soc.* **2013**, *135*, 12684–12689. [[CrossRef](#)] [[PubMed](#)]
13. Lange, A.; Mills, R.E.; Lange, C.J.; Stewart, M.; Devine, S.E.; Corbett, A.H. Classical nuclear localization signals: Definition, function, and interaction with importin α . *J. Biol. Chem.* **2007**, *282*, 5101–5105. [[CrossRef](#)]
14. Sankhala, R.S.; Lokareddy, R.K.; Begum, S.; Pumroy, R.A.; Gillilan, R.E.; Cingolani, G. Three-dimensional context rather than NLS amino acid sequence determines importin α subtype specificity for RCC1. *Nat. Commun.* **2017**, *8*, 979. [[CrossRef](#)]
15. Lu, J.; Wu, T.; Zhang, B.; Liu, S.; Song, W.; Qiao, J.; Ruan, H. Types of nuclear localization signals and mechanisms of protein import into the nucleus. *Cell Commun. Signal.* **2021**, *19*, 60. [[CrossRef](#)] [[PubMed](#)]
16. Atale, N.; Gupta, S.; Yadav, U.C.S.; Rani, V. Cell-death assessment by fluorescent and nonfluorescent cytosolic and nuclear staining techniques. *J. Microsc.* **2014**, *255*, 7–19. [[CrossRef](#)]
17. Massignani, M.; LoPresti, C.; Blanazs, A.; Madsen, J.; Armes, S.P.; Lewis, A.L.; Battaglia, G. Controlling cellular uptake by surface chemistry, size, and surface topology at the nanoscale. *Small* **2009**, *5*, 2424–2432. [[CrossRef](#)]
18. Ploeger, L.; Dullens, H.; Huisman, A.; van Diest, P. Fluorescent stains for quantification of DNA by confocal laser scanning microscopy in 3-D. *Biotech. Histochem.* **2008**, *83*, 63–69. [[CrossRef](#)]
19. Yamauchi, K.; Yang, M.; Jiang, P.; Yamamoto, N.; Xu, M.; Amoh, Y.; Tsuji, K.; Bouvet, M.; Tsuchiya, H.; Tomita, K.; et al. Real-time in vivo dual-color imaging of intracapillary cancer cell and nucleus deformation and migration. *Cancer Res.* **2005**, *65*, 4246–4252. [[CrossRef](#)]
20. Pfeifer, G.P.; You, Y.-H.; Besaratinia, A. Mutations induced by ultraviolet light. *Mutat. Res. Fundam. Mol. Mech. Mutagen.* **2005**, *571*, 19–31. [[CrossRef](#)]
21. Wojcik, K.; Dobrucki, J.W. Interaction of a DNA intercalator DRAQ5, and a minor groove binder SYTO17, with chromatin in live cells—Influence on chromatin organization and histone–DNA interactions. *Cytometry A* **2008**, *73A*, 555–562. [[CrossRef](#)] [[PubMed](#)]
22. Li, C.; Yu, M.; Sun, Y.; Wu, Y.; Huang, C.; Li, F. A nonemissive iridium(III) complex that specifically lights-up the nuclei of living cells. *J. Am. Chem. Soc.* **2011**, *133*, 11231–11239. [[CrossRef](#)]
23. Liu, S.; Liang, H.; Zhang, K.Y.; Zhao, Q.; Zhou, X.; Xu, W.; Huang, W. A multifunctional phosphorescent iridium(III) complex for specific nucleus staining and hypoxia monitoring. *Chem. Commun.* **2015**, *51*, 7943–7946. [[CrossRef](#)] [[PubMed](#)]
24. Gill, M.R.; Garcia-Lara, J.; Foster, S.J.; Smythe, C.; Battaglia, G.; Thomas, J.A. A ruthenium(II) polypyridyl complex for direct imaging of DNA structure in living cells. *Nat. Chem.* **2009**, *1*, 662–667. [[CrossRef](#)]
25. Nakamura, A.; Takigawa, K.; Kurishita, Y.; Kuwata, K.; Ishida, M.; Shimoda, Y.; Hamachi, I.; Tsukiji, S. Hoechst tagging: A modular strategy to design synthetic fluorescent probes for live-cell nucleus imaging. *Chem. Commun.* **2014**, *50*, 6149–6152. [[CrossRef](#)] [[PubMed](#)]
26. Lukinavičius, G.; Blaukopf, C.; Pershagen, E.; Schena, A.; Reymond, L.; Derivery, E.; Gonzalez-Gaitan, M.; D’Este, E.; Hell, S.W.; Wolfram Gerlich, D.; et al. SiR–Hoechst is a far-red DNA stain for live-cell nanoscopy. *Nat. Commun.* **2015**, *6*, 8497. [[CrossRef](#)]
27. Bucevičius, J.; Keller-Findeisen, J.; Gilat, T.; Hell, S.W.; Lukinavičius, G. Rhodamine–Hoechst positional isomers for highly efficient staining of heterochromatin. *Chem. Sci.* **2019**, *10*, 1962–1970. [[CrossRef](#)]
28. Zhang, X.; Ye, Z.; Zhang, X.; Man, H.; Huang, Z.; Li, N.; Xiao, Y. A targetable fluorescent probe for dSTORM super-resolution imaging of live cell nucleus DNA. *Chem. Commun.* **2019**, *55*, 1951–1954. [[CrossRef](#)] [[PubMed](#)]

29. Peng, X.; Wu, T.; Fan, J.; Wang, J.; Zhang, S.; Song, F.; Sun, S. An effective minor groove binder as a red fluorescent marker for live-cell DNA imaging and quantification. *Angew. Chem. Int. Ed.* **2011**, *50*, 4180–4183. [[CrossRef](#)]
30. Zhang, S.; Fan, J.; Li, Z.; Hao, N.; Cao, J.; Wu, T.; Wang, J.; Peng, X. A bright red fluorescent cyanine dye for live-cell nucleic acid imaging, with high photostability and a large Stokes shift. *J. Mater. Chem. B* **2014**, *2*, 2688–2693. [[CrossRef](#)]
31. Lu, Y.-J.; Deng, Q.; Hu, D.-P.; Wang, Z.-Y.; Huang, B.-H.; Du, Z.-Y.; Fang, Y.-X.; Wong, W.-L.; Zhang, K.; Chow, C.-F. A molecular fluorescent dye for specific staining and imaging of RNA in live cells: A novel ligand integration from classical thiazole orange and styryl compounds. *Chem. Commun.* **2015**, *51*, 15241–15244. [[CrossRef](#)]
32. Kurutos, A.; Ilic-Tomic, T.; Kamounah, F.S.; Vasilev, A.A.; Nikodinovic-Runic, J. Non-cytotoxic photostable monomethine cyanine platforms: Combined paradigm of nucleic acid staining and in vivo imaging. *J. Photochem. Photobiol. A* **2020**, *397*, 112598. [[CrossRef](#)]
33. Kurutos, A.; Nikodinovic-Runic, J.; Veselinovic, A.; Veselinović, J.B.; Kamounah, F.S.; Ilic-Tomic, T. RNA-targeting low-molecular-weight fluorophores for nucleoli staining: Synthesis, in silico modelling and cellular imaging. *New J. Chem.* **2021**, *45*, 12818–12829. [[CrossRef](#)]
34. Aristova, D.; Kosach, V.; Chernii, S.; Slominsky, Y.; Balanda, A.; Filonenko, V.; Yarmoluk, S.; Rotaru, A.; Özkan, H.G.; Mokhir, A.; et al. Monomethine cyanine probes for visualization of cellular RNA by fluorescence microscopy. *Methods Appl. Fluoresc.* **2021**, *9*, 045002. [[CrossRef](#)]
35. Aristova, D.; Selin, R.; Heil, H.S.; Kosach, V.; Slominsky, Y.; Yarmoluk, S.; Pekhnyo, V.; Kovalska, V.; Henriques, R.; Mokhir, A.; et al. Trimethine cyanine dyes as NA-sensitive probes for visualization of cell compartments in fluorescence microscopy. *ACS Omega* **2022**, *7*, 47734–47746. [[CrossRef](#)]
36. Zhou, B.; Liu, W.; Zhang, H.; Wu, J.; Liu, S.; Xu, H.; Wang, P. Imaging of nucleolar RNA in living cells using a highly photostable deep-red fluorescent probe. *Biosens. Bioelectron.* **2015**, *68*, 189–196. [[CrossRef](#)]
37. Liu, W.; Zhou, B.; Niu, G.; Ge, J.; Wu, J.; Zhang, H.; Xu, H.; Wang, P. Deep-red emissive crescent-shaped fluorescent dyes: Substituent effect on live cell imaging. *ACS Appl. Mater. Interfaces* **2015**, *7*, 7421–7427. [[CrossRef](#)] [[PubMed](#)]
38. Boynton, A.N.; Marcélis, L.; Barton, J.K. $[\text{Ru}(\text{Me}_4\text{phen})_2\text{dppz}]^{2+}$, a light switch for DNA mismatches. *J. Am. Chem. Soc.* **2016**, *138*, 5020–5023. [[CrossRef](#)] [[PubMed](#)]
39. Boynton, A.N.; Marcélis, L.; McConnell, A.J.; Barton, J.K. A ruthenium(ii) complex as a luminescent probe for DNA mismatches and abasic sites. *Inorg. Chem.* **2017**, *56*, 8381–8389. [[CrossRef](#)] [[PubMed](#)]
40. Nano, A.; Boynton, A.N.; Barton, J.K. A rhodium-cyanine fluorescent probe: Detection and signaling of mismatches in DNA. *J. Am. Chem. Soc.* **2017**, *139*, 17301–17304. [[CrossRef](#)] [[PubMed](#)]
41. Sun, X.; Lei, Y. Fluorescent carbon dots and their sensing applications. *TrAC Trends Anal. Chem.* **2017**, *89*, 163–180. [[CrossRef](#)]
42. Hong, G.; Diao, S.; Antaris, A.L.; Dai, H. Carbon nanomaterials for biological imaging and nanomedicinal therapy. *Chem. Rev.* **2015**, *115*, 10816–10906. [[CrossRef](#)]
43. Serdiuk, T.; Lysenko, V.; Mognetti, B.; Skryshevsky, V.; Géloën, A. Impact of cell division on intracellular uptake and nuclear targeting with fluorescent SiC-based nanoparticles. *J. Biophotonics* **2013**, *6*, 291–297. [[CrossRef](#)] [[PubMed](#)]
44. Han, G.; Zhao, J.; Zhang, R.; Tian, X.; Liu, Z.; Wang, A.; Liu, R.; Liu, B.; Han, M.-Y.; Gao, X.; et al. Membrane-penetrating carbon quantum dots for imaging nucleic acid structures in live organisms. *Angew. Chem. Int. Ed.* **2019**, *58*, 7087–7091. [[CrossRef](#)] [[PubMed](#)]
45. Feng, X.J.; Wu, P.L.; Bolze, F.; Leung, H.W.C.; Li, K.F.; Mak, N.K.; Kwong, D.W.J.; Nicoud, J.-F.; Cheah, K.W.; Wong, M.S. Cyanines as new fluorescent probes for DNA detection and two-photon excited bioimaging. *Org. Lett.* **2010**, *12*, 2194–2197. [[CrossRef](#)] [[PubMed](#)]
46. Zheng, Y.-C.; Zheng, M.-L.; Chen, S.; Zhao, Z.-S.; Duan, X.-M. Biscarbazolylmethane-based cyanine: A two-photon excited fluorescent probe for DNA and selective cell imaging. *J. Mater. Chem. B* **2014**, *2*, 2301–2310. [[CrossRef](#)] [[PubMed](#)]
47. Allain, C.; Schmidt, F.; Lartia, R.; Bordeau, G.; Fiorini-Debuisschert, C.; Charra, F.; Tauc, P.; Teulade-Fichou, M.-P. Vinylpyridinium triphenylamines: Novel far-red emitters with high photostability and two-photon absorption properties for staining DNA. *Chembiochem* **2007**, *8*, 424–433. [[CrossRef](#)]
48. Gaur, P.; Kumar, A.; Dey, G.; Kumar, R.; Bhattacharyya, S.; Ghosh, S. Selenium incorporated cationic organochalcogen: Live cell compatible and highly photostable molecular stain for imaging and localization of intracellular DNA. *ACS Appl. Mater. Interfaces* **2016**, *8*, 10690–10699. [[CrossRef](#)] [[PubMed](#)]
49. Wu, J.; Zou, Y.; Li, C.; Sicking, W.; Piantanida, I.; Yi, T.; Schmuck, C. A molecular peptide beacon for the ratiometric sensing of nucleic acids. *J. Am. Chem. Soc.* **2012**, *134*, 1958–1961. [[CrossRef](#)]
50. Liu, L.-Y.; Zhao, Y.; Zhang, N.; Wang, K.-N.; Tian, M.; Pan, Q.; Lin, W. Ratiometric fluorescence imaging for the distribution of nucleic acid content in living cells and human tissue sections. *Anal. Chem.* **2021**, *93*, 1612–1619. [[CrossRef](#)]
51. Suseela, Y.V.; Narayanaswamy, N.; Pratihari, S.; Govindaraju, T. Far-red fluorescent probes for canonical and non-canonical nucleic acid structures: Current progress and future implications. *Chem. Soc. Rev.* **2018**, *47*, 1098–1131. [[CrossRef](#)]
52. Yao, Q.; Li, H.; Xian, L.; Xu, F.; Xia, J.; Fan, J.; Du, J.; Wang, J.; Peng, X. Differentiating RNA from DNA by a molecular fluorescent probe based on the “door-bolt” mechanism biomaterials. *Biomaterials* **2018**, *177*, 78–87. [[CrossRef](#)] [[PubMed](#)]
53. Yoshino, Y.; Sato, Y.; Nishizawa, S. Deep-red light-up signaling of benzo[c,d]indole–quinoline monomethine cyanine for imaging of nucleolar RNA in living cells and for sequence-selective RNA analysis. *Anal. Chem.* **2019**, *91*, 14254–14260. [[CrossRef](#)] [[PubMed](#)]

54. Cao, C.; Wei, P.; Li, R.; Zhong, Y.; Li, X.; Xue, F.; Shi, Y.; Yi, T. Ribosomal RNA-selective light-up fluorescent probe for rapidly imaging the nucleolus in live cells. *ACS Sens.* **2019**, *4*, 1409–1416. [[CrossRef](#)] [[PubMed](#)]
55. Liu, Y.; Niu, J.; Wang, W.; Lin, W. Tracking of mitochondrial endogenous ribonucleic acid in the cancer cells and macrophages using a novel small-molecular fluorescent probe. *Anal. Chem.* **2019**, *91*, 1715–1718. [[CrossRef](#)] [[PubMed](#)]
56. Liu, Y.; Zhang, W.; Sun, Y.; Song, G.; Miao, F.; Guo, F.; Tian, M.; Yu, X.; Sun, J.Z. Two-photon fluorescence imaging of RNA in nucleoli and cytoplasm in living cells based on low molecular weight probes. *Dyes Pigm.* **2014**, *103*, 191–201. [[CrossRef](#)]
57. Liu, J.; Zhang, S.; Zhang, C.; Dong, J.; Shen, C.; Zhu, J.; Xu, H.; Fu, M.; Yang, G.; Zhang, X. A water-soluble two-photon ratiometric triarylboron probe with nucleolar targeting by preferential RNA binding. *Chem. Commun.* **2017**, *53*, 11476–11479. [[CrossRef](#)]
58. Lu, Y.-J.; Deng, Q.; Hou, J.-Q.; Hu, D.-P.; Wang, Z.-Y.; Zhang, K.; Luyt, L.G.; Wong, W.-L.; Chow, C.-F. Molecular engineering of thiazole orange dye: Change of fluorescent signaling from universal to specific upon binding with nucleic acids in bioassay. *ACS Chem. Biol.* **2016**, *11*, 1019–1029. [[CrossRef](#)]
59. Grande, V.; Doria, F.; Freccero, M.; Würthner, F. An aggregating amphiphilic squaraine: A light-up probe that discriminates parallel G-quadruplexes. *Angew. Chem. Int. Ed.* **2017**, *56*, 7520–7524. [[CrossRef](#)]
60. Grande, V.; Shen, C.-A.; Deiana, M.; Dudek, M.; Olesiak-Banska, J.; Matczyszyn, K.; Würthner, F. Selective parallel G-quadruplex recognition by a NIR-to-NIR two-photon squaraine. *Chem. Sci.* **2018**, *9*, 8375–8381. [[CrossRef](#)]
61. Yang, F.; Zuo, X.; Fan, C.; Zhang, X.-E. Biomacromolecular nanostructures-based interfacial engineering: From precise assembly to precision biosensing. *Natl. Sci. Rev.* **2018**, *5*, 740–755. [[CrossRef](#)]
62. Choi, J.; Majima, T. Conformational changes of non-B DNA. *Chem. Soc. Rev.* **2011**, *40*, 5893–5909. [[CrossRef](#)] [[PubMed](#)]
63. Stelson, A.C.; Liu, M.; Little, C.A.E.; Long, C.J.; Orloff, N.D.; Stephanopoulos, N.; Booth, J.C. Label-free detection of conformational changes in switchable DNA nanostructures with microwave microfluidics. *Nat. Commun.* **2019**, *10*, 1174. [[CrossRef](#)] [[PubMed](#)]
64. Parkinson, G.N.; Lee, M.P.H.; Neidle, S. Crystal structure of parallel quadruplexes from human telomeric DNA. *Nature* **2002**, *417*, 876–880. [[CrossRef](#)] [[PubMed](#)]
65. Chen, B.; Huang, Q.; Qu, Z.; Li, C.; Li, Q.; Shi, J.; Fan, C.; Wang, L.; Zuo, X.; Shen, J.; et al. Probing transient DNA conformation changes with an intercalative fluorescent excimer. *Angew. Chem. Int. Ed.* **2021**, *60*, 6624–6630. [[CrossRef](#)]
66. Ye, Z.; Yu, H.; Yang, W.; Zheng, Y.; Li, N.; Bian, H.; Wang, Z.; Liu, Q.; Song, Y.; Zhang, M.; et al. Strategy to lengthen the on-time of photochromic rhodamine spirolactam for super-resolution photoactivated localization microscopy. *J. Am. Chem. Soc.* **2019**, *141*, 6527–6536. [[CrossRef](#)]
67. Tsankova, N.; Renthal, W.; Kumar, A.; Nestler, E.J. Epigenetic regulation in psychiatric disorders. *Nat. Rev. Neurosci.* **2007**, *8*, 355–367. [[CrossRef](#)]
68. Minoshima, M.; Matsumoto, T.; Kikuchi, K. Development of a fluorogenic probe based on a DNA staining dye for continuous monitoring of the histone deacetylase reaction. *Anal. Chem.* **2014**, *86*, 7925–7930. [[CrossRef](#)]
69. Rooker, D.R.; Buccella, D. Real-time detection of histone deacetylase activity with a small molecule fluorescent and spectrophotometric probe. *Chem. Sci.* **2015**, *6*, 6456–6461. [[CrossRef](#)]
70. Chao, D.; Ni, S. Nanomolar pyrophosphate detection and nucleus staining in living cells with simple terpyridine–Zn(II) complexes. *Sci. Rep.* **2016**, *6*, 26477. [[CrossRef](#)]
71. Clayson, D.B.; Mehta, R.; Iverson, F. Oxidative DNA damage—The effects of certain genotoxic and operationally non-genotoxic carcinogens. *Mutat. Res./Rev. Gene. Toxic.* **1994**, *317*, 25–42. [[CrossRef](#)] [[PubMed](#)]
72. Loft, S.; Poulsen, H.E. Cancer risk and oxidative DNA damage in man. *J. Mol. Med.* **1996**, *74*, 297–312. [[CrossRef](#)] [[PubMed](#)]
73. Dickinson, B.C.; Tang, Y.; Chang, Z.; Chang, C.J. A nuclear-localized fluorescent hydrogen peroxide probe for monitoring sirtuin-mediated oxidative stress responses in vivo. *Chem. Biol.* **2011**, *18*, 943–948. [[CrossRef](#)] [[PubMed](#)]
74. Wen, Y.; Liu, K.; Yang, H.; Li, Y.; Lan, H.; Liu, Y.; Zhang, X.; Yi, T. A highly sensitive ratiometric fluorescent probe for the detection of cytoplasmic and nuclear hydrogen peroxide. *Anal. Chem.* **2014**, *86*, 9970–9976. [[CrossRef](#)]
75. Ozmen, B.; Akkaya, E.U. Infrared fluorescence sensing of submicromolar calcium: Pushing the limits of photoinduced electron transfer. *Tetrahedron Lett.* **2000**, *41*, 9185–9188. [[CrossRef](#)]
76. Zhu, B.; Jia, H.; Zhang, X.; Chen, Y.; Liu, H.; Tan, W. Engineering a subcellular targetable, red-emitting, and ratiometric fluorescent probe for Ca²⁺ and its bioimaging applications. *Anal. Bioanal. Chem.* **2010**, *397*, 1245–1250. [[CrossRef](#)]
77. Li, W.-H.; Fraser, S.E.; Meade, T.J. A calcium-sensitive magnetic resonance imaging contrast agent. *J. Am. Chem. Soc.* **1999**, *121*, 1413–1414. [[CrossRef](#)]
78. Tatay, S.; Gaviña, P.; Coronado, E.; Palomares, E. Optical mercury sensing using a benzothiazolium hemicyanine dye. *Org. Lett.* **2006**, *8*, 3857–3860. [[CrossRef](#)]
79. Wang, K.-N.; Liu, L.-Y.; Mao, D.; Hou, M.-X.; Tan, C.-P.; Mao, Z.-W.; Liu, B. A nuclear-targeted AIE photosensitizer for enzyme inhibition and photosensitization in cancer cell ablation. *Angew. Chem. Int. Ed.* **2022**, *61*, e202114600.
80. Zhang, P.; Huang, H.; Banerjee, S.; Clarkson, G.J.; Ge, C.; Imberti, C.; Sadler, P.J. Nucleus-targeted organoiridium–albumin conjugate for photodynamic cancer therapy. *Angew. Chem. Int. Ed.* **2019**, *58*, 2350–2354. [[CrossRef](#)]
81. Sharma, B.R. Infection in patients with severe burns: Causes and prevention thereof. *Infect. Dis. Clin. N. Am.* **2007**, *21*, 745–759. [[CrossRef](#)] [[PubMed](#)]
82. Gao, Y.; Wang, X.; He, X.; He, Z.; Yang, X.; Tian, S.; Meng, F.; Ding, D.; Luo, L.; Tang, B.Z. A dual-functional photosensitizer for ultraefficient photodynamic therapy and synchronous anticancer efficacy monitoring. *Adv. Funct. Mater.* **2019**, *29*, 1902673. [[CrossRef](#)]

83. Zhang, T.; Li, Y.; Zheng, Z.; Ye, R.; Zhang, Y.; Kwok, R.T.K.; Lam, J.W.Y.; Tang, B.Z. In situ monitoring apoptosis process by a self-reporting photosensitizer. *J. Am. Chem. Soc.* **2019**, *141*, 5612–5616. [[CrossRef](#)] [[PubMed](#)]
84. Cheng, Y.; Sun, C.; Liu, R.; Yang, J.; Dai, J.; Zhai, T.; Lou, X.; Xia, F. A multifunctional peptide-conjugated AIEgen for efficient and sequential targeted gene delivery into the nucleus. *Angew. Chem. Int. Ed.* **2019**, *58*, 5049–5053. [[CrossRef](#)]
85. Burke, C.S.; Byrne, A.; Keyes, T.E. Targeting photoinduced DNA destruction by Ru(II) tetraazaphenanthrene in live cells by signal peptide. *J. Am. Chem. Soc.* **2018**, *140*, 6945–6955. [[CrossRef](#)]
86. Song, H.; Allison, S.J.; Brabec, V.; Bridgewater, H.E.; Kasparkova, J.; Kosthunova, H.; Novohradsky, V.; Phillips, R.M.; Pracharova, J.; Rogers, N.J.; et al. Glycoconjugated metallohelices have improved nuclear delivery and suppress tumour growth in vivo. *Angew. Chem. Int. Ed.* **2020**, *59*, 14677–14685. [[CrossRef](#)]
87. Cheng, H.; Fan, J.-H.; Zhao, L.-P.; Fan, G.-L.; Zheng, R.-R.; Qiu, X.-Z.; Yu, X.-Y.; Li, S.-Y.; Zhang, X.-Z. Chimeric peptide engineered exosomes for dual-stage light guided plasma membrane and nucleus targeted photodynamic therapy. *Biomaterials* **2019**, *211*, 14–24. [[CrossRef](#)] [[PubMed](#)]
88. Pan, L.; He, Q.; Liu, J.; Chen, Y.; Ma, M.; Zhang, L.; Shi, J. Nuclear-targeted drug delivery of TAT peptide-conjugated monodisperse mesoporous silica nanoparticles. *J. Am. Chem. Soc.* **2012**, *134*, 5722–5725. [[CrossRef](#)]
89. KC, R.B.; Thapa, B.; Xu, P. pH and redox dual responsive nanoparticle for nuclear targeted drug delivery. *Mol. Pharm.* **2012**, *9*, 2719–2729.
90. Yang, Y.; Zhu, W.; Feng, L.; Chao, Y.; Yi, X.; Dong, Z.; Yang, K.; Tan, W.; Liu, Z.; Chen, M. G-quadruplex-based nanoscale coordination polymers to modulate tumor hypoxia and achieve nuclear-targeted drug delivery for enhanced photodynamic therapy. *Nano Lett.* **2018**, *18*, 6867–6875. [[CrossRef](#)]
91. Chen, W.; Liu, J.; Wang, Y.; Jiang, C.; Yu, B.; Sun, Z.; Lu, L. A C₅N₂ nanoparticle based direct nucleus delivery platform for synergistic cancer therapy. *Angew. Chem. Int. Ed.* **2019**, *58*, 6290–6294. [[CrossRef](#)]
92. Lei, Z.; Ding, L.; Yao, C.; Mo, F.; Li, C.; Huang, Y.; Yin, X.; Li, M.; Liu, J.; Zhang, Y.; et al. A highly efficient tumor-targeting nanoprobe with a novel cell membrane permeability mechanism. *Adv. Mater.* **2019**, *31*, 1807456. [[CrossRef](#)]

Disclaimer/Publisher's Note: The statements, opinions and data contained in all publications are solely those of the individual author(s) and contributor(s) and not of MDPI and/or the editor(s). MDPI and/or the editor(s) disclaim responsibility for any injury to people or property resulting from any ideas, methods, instructions or products referred to in the content.